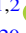


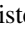

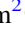






# Deep Exploration of $\epsilon$ Eridani with Keck *Ms*-band Vortex Coronagraphy and Radial Velocities: Mass and Orbital Parameters of the Giant Exoplanet\*

Dimitri Mawet<sup>1,2</sup> , Lea Hirsch<sup>3,4</sup> , Eve J. Lee<sup>5</sup> , Jean-Baptiste Ruffio<sup>6</sup> , Michael Bottom<sup>2</sup> , Benjamin J. Fulton<sup>7</sup> , Olivier Absil<sup>8,20</sup> , Charles Beichman<sup>2,9,10</sup> , Brendan Bowler<sup>11</sup> , Marta Bryan<sup>1</sup> , Elodie Choquet<sup>1,21</sup> , David Ciardi<sup>7</sup> , Valentin Christiaens<sup>8,12,13</sup> , Denis Defrère<sup>8</sup> , Carlos Alberto Gomez Gonzalez<sup>14</sup> , Andrew W. Howard<sup>1</sup> , Elsa Huby<sup>15</sup> , Howard Isaacson<sup>4</sup> , Rebecca Jensen-Clem<sup>4,22</sup> , Molly Kosiarek<sup>16,23</sup> , Geoff Marcy<sup>4</sup> , Tiffany Meshkat<sup>17</sup> , Erik Petigura<sup>1</sup> , Maddalena Reggiani<sup>8</sup> , Garreth Ruane<sup>1,24</sup> , Eugene Serabyn<sup>2</sup> , Evan Sinukoff<sup>18</sup> , Ji Wang<sup>1</sup> , Lauren Weiss<sup>19</sup> , and Marie Ygouf<sup>17</sup>

<sup>1</sup> Department of Astronomy, California Institute of Technology, Pasadena, CA 91125, USA; [dmawet@astro.caltech.edu](mailto:dmawet@astro.caltech.edu)

<sup>2</sup> Jet Propulsion Laboratory, California Institute of Technology, Pasadena, CA 91109, USA

<sup>3</sup> Kavli Institute for Particle Astrophysics and Cosmology, Stanford University, Stanford, CA 94305, USA

<sup>4</sup> University of California, Berkeley, 510 Campbell Hall, Astronomy Department, Berkeley, CA 94720, USA

<sup>5</sup> TAPIR, Walter Burke Institute for Theoretical Physics, Mailcode 350-17, Caltech, Pasadena, CA 91125, USA

<sup>6</sup> Kavli Institute for Particle Astrophysics and Cosmology, Stanford University, Stanford, CA 94305, USA

<sup>7</sup> NASA Exoplanet Science Institute, Caltech/IPAC-NExSci, 1200 East California Boulevard, Pasadena, CA 91125, USA

<sup>8</sup> Space sciences, Technologies & Astrophysics Research (STAR) Institute, Université de Liège, Allée du Six Août 19c, B-4000 Sart Tilman, Belgium

<sup>9</sup> Division of Physics, Mathematics, and Astronomy, California Institute of Technology, Pasadena, CA 91125, USA

<sup>10</sup> NASA Exoplanet Science Institute, 770 S. Wilson Avenue, Pasadena, CA 911225, USA

<sup>11</sup> McDonald Observatory and the University of Texas at Austin, Department of Astronomy, 2515 Speedway, Stop C1400, Austin, TX 78712, USA

<sup>12</sup> Departamento de Astronomía, Universidad de Chile, Casilla 36-D, Santiago, Chile

<sup>13</sup> Millennium Nucleus “Protoplanetary Disks in ALMA Early Science,” Chile

<sup>14</sup> Université Grenoble Alpes, IPAG, F-38000 Grenoble, France

<sup>15</sup> LESIA, Observatoire de Paris, Meudon, France

<sup>16</sup> University of California, Santa Cruz; Department of Astronomy and Astrophysics, Santa Cruz, CA 95064, USA

<sup>17</sup> IPAC, California Institute of Technology, M/C 100-22, 770 S. Wilson Ave, Pasadena, CA 91125, USA

<sup>18</sup> Institute for Astronomy, University of Hawai’i at Manoa, Honolulu, HI 96822, USA

<sup>19</sup> Institut de Recherche sur les Exoplanètes, Département de Physique, Université de Montréal, C.P. 6128, Succ. Centre-ville, Montréal, QC H3C 3J7, Canada

Received 2018 May 1; revised 2018 October 16; accepted 2018 October 29; published 2019 January 3

## Abstract

We present the most sensitive direct imaging and radial velocity (RV) exploration of  $\epsilon$  Eridani to date.  $\epsilon$  Eridani is an adolescent planetary system, reminiscent of the early solar system. It is surrounded by a prominent and complex debris disk that is likely stirred by one or several gas giant exoplanets. The discovery of the RV signature of a giant exoplanet was announced 15 yr ago, but has met with scrutiny due to possible confusion with stellar noise. We confirm the planet with a new compilation and analysis of precise RV data spanning 30 yr, and combine it with upper limits from our direct imaging search, the most sensitive ever performed. The deep images were taken in the *Ms* band (4.7  $\mu$ m) with the vortex coronagraph recently installed in W.M. Keck Observatory’s infrared camera NIRC2, which opens a sensitive window for planet searches around nearby adolescent systems. The RV data and direct imaging upper limit maps were combined in an innovative joint Bayesian analysis, providing new constraints on the mass and orbital parameters of the elusive planet.  $\epsilon$  Eridani b has a mass of  $0.78^{+0.38}_{-0.12} M_{\text{Jup}}$  and is orbiting  $\epsilon$  Eridani at about  $3.48 \pm 0.02$  au with a period of  $7.37 \pm 0.07$  yr. The eccentricity of  $\epsilon$  Eridani b’s orbit is  $0.07^{+0.06}_{-0.05}$ , an order of magnitude smaller than early estimates and consistent with a circular orbit. We discuss our findings from the standpoint of planet–disk interactions and prospects for future detection and characterization with the *James Webb Space Telescope*.

**Key words:** planet–disk interactions – planets and satellites: dynamical evolution and stability – planets and satellites: gaseous planets – stars: planetary systems – techniques: high angular resolution – techniques: radial velocities

**Supporting material:** machine-readable tables

## 1. Introduction

$\epsilon$  Eridani is an adolescent (200–800 Myr) (Fuhrmann 2004; Mamajek & Hillenbrand 2008) K2V dwarf star (Table 1). At a distance of 3.2 pc,  $\epsilon$  Eridani is the tenth closest star to the Sun, which makes it a particularly attractive target for deep planet searches. Its age, spectral type, distance, and consequent apparent brightness ( $V = 3.73$  mag) make it a benchmark system, as well as an excellent analog for the early phases of the solar system’s evolution.  $\epsilon$  Eridani hosts a prominent, complex debris disk, and a putative Jupiter-like planet.

\* Based on observations obtained at the W. M. Keck Observatory, which is operated jointly by the University of California and the California Institute of Technology. Keck time was granted for this project by Caltech, the University of Hawai’i, the University of California, and NASA.

<sup>20</sup> F.R.S.–FNRS Research Associate.

<sup>21</sup> Hubble Postdoctoral Fellow.

<sup>22</sup> Miller Fellow.

<sup>23</sup> NSF Graduate Research Fellow.

<sup>24</sup> NSF Astronomy and Astrophysics Postdoctoral Fellow.

**Table 1**  
Properties of  $\epsilon$  Eridani

| Property             | Value               | References                   |
|----------------------|---------------------|------------------------------|
| R.A. (hms)           | 03 32 55.8 (J2000)  | van Leeuwen (2007)           |
| Decl. (dms)          | -09 27 29.7 (J2000) | van Leeuwen (2007)           |
| Spect. type          | K2V                 | Keenan & McNeil (1989)       |
| Mass ( $M_{\odot}$ ) | $0.781 \pm 0.005$   | Boyajian et al. (2012)       |
| Distance (pc)        | $3.216 \pm 0.0015$  | van Leeuwen (2007)           |
| $V$ mag              | 3.73                | Ducati (2002)                |
| $K$ mag              | 1.67                | Ducati (2002)                |
| $L$ mag              | 1.60                | Cox (2000)                   |
| $M$ mag              | 1.69                | Cox (2000)                   |
| Age (Myr)            | 200–800             | Mamajek & Hillenbrand (2008) |

### 1.1. $\epsilon$ Eridani’s Debris Disk

The disk was first detected by the *Infrared Astronomical Satellite* (Aumann 1985) and later on by the *Infrared Space Observatory* (Walker & Heinrichsen 2000). It was first imaged by the Submillimetre Common-User Bolometer Array (SCUBA) at the James Clerk Maxwell Telescope by Greaves et al. (1998).  $\epsilon$  Eridani is one of the “fabulous four” Vega-like debris disks and shows more than 1 Jy of far-infrared (FIR) excess over the stellar photosphere at 60–200  $\mu\text{m}$  and a lower significance excess at 25  $\mu\text{m}$  (Aumann 1985). Using the *Spitzer Space Telescope* and the Caltech Submillimeter Observatory (CSO) to trace  $\epsilon$  Eridani’s spectral energy distribution (SED) from 3.5 to 350  $\mu\text{m}$ , the model presented in Backman et al. (2009) paints a complex picture.  $\epsilon$  Eridani’s debris disk is composed of a main ring at 35–90 au, and a set of two narrow inner dust belts inside the cavity delineated by the outer ring: one belt with a color temperature  $T \simeq 55$  K at approximately 20 au, and another belt with a color temperature  $T \simeq 120$  K at approximately 3 au (Backman et al. 2009). The authors argue that, to maintain the three-belt system around  $\epsilon$  Eridani, three shepherding planets are necessary.

Using *Herschel* at 70, 160, 250, 350, and 500  $\mu\text{m}$ , Greaves et al. (2014) refined the position and the width of the outer belt to be 54–68 au, but only resolved one of the inner belts at 12–16 au. More recently, Chavez-Dagostino et al. (2016) used the Large Millimetre Telescope Alfonso Serrano (LMT) at 1.1 mm and resolved the outer belt at a separation of 64 au. Emission is detected at the location of the star in excess of the photosphere. The angular resolution of the 1.1 mm map, however, is not sufficient to resolve the inner two warm belts of Backman et al. (2009). MacGregor et al. (2015) used the Submillimeter Array (SMA) at 1.3 mm and the Australia Telescope Compact Array (ATCA) at 7 mm to resolve the outer ring and measure its width (measurement now superseded by ALMA, see below). The data at both mm wavelengths show excess emission, which the authors attribute to ionized plasma from a stellar corona or chromosphere.

Su et al. (2017) recently presented 35  $\mu\text{m}$  images of  $\epsilon$  Eridani obtained with the Stratospheric Observatory for Infrared Astronomy (SOFIA). The inner disk system is marginally resolved within 25 au. Combining the 15–38  $\mu\text{m}$  excess spectrum with *Spitzer* data, Su et al. (2017) find that the presence of in situ dust-producing planetesimal belt(s) is the most likely source of the infrared excess emission in the inner 25 au region. However, the SOFIA data are not constraining enough to distinguish one broad inner disk from two narrow belts.

Booth et al. (2017) used the Atacama Large Millimeter/submillimeter Array (ALMA) to image the northern arc of the outer ring at high angular resolution (beam size  $< 2''$ ). The 1.34 mm continuum image has a low signal-to-noise ratio (S/N) but is well-resolved, with the outer ring extending from 62.6 to 75.9 au. The fractional outer disk width is comparable to that of the solar system’s Kuiper Belt and makes it one of the narrowest debris disks known, with a width of just  $\simeq 12$  au. The outer ring inclination is measured to be  $i = 34^{\circ} \pm 2^{\circ}$ , consistent with all previous estimates using lower-resolution submm facilities (Greaves et al. 1998, 2005; Backman et al. 2009). No significant emission is detected between  $\sim 20$  and  $\sim 60$  au (see Booth et al. (2017), their Figure 5), suggesting a large clearing between the inner belt(s) within 20 au and the outer belt outward of 60 au. Booth et al. (2017) find tentative evidence for clumps in the ring, and claim that the inner and outer edges are defined by resonances with a planet at a semimajor axis of 48 au. The authors also confirm the previous detection of unresolved mm emission at the location of the star that is above the level of the photosphere and attribute this excess to stellar chromospheric emission, as suggested by MacGregor et al. (2015). However, the chromospheric emission cannot reproduce the infrared excess seen by *Spitzer* and SOFIA.

Finally, recent 11  $\mu\text{m}$  observations with the Large Binocular Telescope Interferometer (LBTI) suggest that warm dust is present within  $\sim 500$  mas (or 1.6 au) from  $\epsilon$  Eridani (Ertel et al. 2018). The trend of the detected signal with respect to the stellocentric distance also indicates that the bulk of the emission comes from the outer part of the LBTI field of view, and hence is likely associated with the dust belt(s) responsible for the 15–38  $\mu\text{m}$  emission detected by *Spitzer* and SOFIA.

### 1.2. $\epsilon$ Eridani’s Putative Planet

Hatzes et al. (2000) demonstrated that the most likely explanation for the observed decade-long radial velocity (RV) variations was the presence of a  $\simeq 1.5 M_J$  giant planet with a period  $P = 6.9$  yr ( $\simeq 3$  au orbit) and a high eccentricity ( $e = 0.6$ ). While most of the exoplanet community seems to have acknowledged the existence of  $\epsilon$  Eridani b, there is still a possibility that the measured RV variations are due to stellar activity cycles (Anglada-Escudé & Butler 2012; Zechmeister et al. 2013). Backman et al. (2009) rightly noted that a giant planet with this orbit would quickly clear the inner region not only of dust particles but also the parent planetesimal belt needed to resupply them, inconsistent with their observations.

### 1.3. This Paper

In this paper, we present the deepest direct imaging reconnaissance of  $\epsilon$  Eridani to date, a compilation of precision RV measurements spanning 30 years, and an innovative joint Bayesian analysis combining both planet detection methods. Our results place the tightest constraints yet on the planetary mass and orbital parameters for this intriguing planetary system. The paper is organized as follows: Section 2 describes the RV observations and data analysis, Section 3 describes the high-contrast imaging observations and post-processing, Section 4 presents our nondetection and robust detection limits from direct imaging, additional tests on the RV data, and our joint analysis of both data sets. In Section 5, we discuss our findings, the consequences of the new planet parameters on

planet–disk interactions, and prospects for detection with the *James Webb Space Telescope*, before concluding in Section 6.

## 2. Doppler Spectroscopy

In this section, we present our new compilation and analysis of Doppler velocimetry data of  $\epsilon$  Eridani spanning 30 yr.

### 2.1. RV Observations

$\epsilon$  Eridani has been included in planet search programs at both Keck Observatory using the HIRES Spectrometer (Howard et al. 2010) and at Lick Observatory using the Automated Planet Finder (APF) and Levy Spectrometer.  $\epsilon$  Eridani was observed on 206 separate nights with HIRES and the APF, over the past 7 yr.

Keck/HIRES (Vogt et al. 1994) RV observations were obtained starting in 2010, using the standard iodine cell configuration of the California Planet Survey (CPS) (Howard et al. 2010). During the subsequent 7 yr, 91 observations were taken through the B5 or C2 deckers ( $0''.87 \times 3''.5$ , and  $0''.87 \times 14''$ , respectively), yielding a spectral resolution of  $R \approx 55,000$  for each observation. Each measurement was taken through a cell of gaseous molecular iodine heated to  $50^\circ\text{C}$ , which imprints a dense forest of iodine absorption lines onto the stellar spectrum in the spectral region of  $5000\text{--}6200 \text{ \AA}$ . This iodine spectrum was used for wavelength calibration and as a PSF reference. Each RV exposure was timed to yield a per-pixel S/N of  $\gtrsim 200$  at  $550 \text{ nm}$ , with typical exposure times of only a few seconds due to the brightness of the target. An iodine-free template spectrum was obtained using the B3 decker ( $0''.57 \times 14''$ ,  $R \approx 72,000$ ) on 2010 August 30.

RV observations using the APF and Levy Spectrograph (Radovan et al. 2014; Vogt et al. 2014) were taken starting in late 2013. The APF is a 2.4 m telescope dedicated to performing RV detection and follow-up of planets and planet candidates, also using the iodine cell method of wavelength calibration. APF data on  $\epsilon$  Eridani were primarily taken through the W decker ( $1'' \times 3''$ ), with a spectral resolution of  $R \approx 110,000$ . Exposures were typically between 10 and 50 s long, yielding S/N per-pixel of 140. The typical observing strategy at the APF was to take three consecutive exposures and then bin them to average over short-term fluctuations from stellar oscillations. On some nights, more than one triple-exposure was taken. These were binned on a nightly timescale. An iodine-free template consisting of five consecutive exposures was obtained on 2014 February 17 using the N decker ( $0''.5 \times 8''$ ) with resolution  $R \approx 150,000$ . Both the APF and HIRES RVs were calibrated to the solar system barycenter and corrected for the changing perspective caused by the high proper motion of  $\epsilon$  Eridani.

In addition to the new HIRES and APF RV data, we incorporate previously published data from several telescopes into this study. High-precision RV observations of  $\epsilon$  Eridani were taken with the Hamilton spectrograph at Lick Observatory starting in 1987, as part of the Lick Planet Search program. They were published in the catalog of Fischer et al. (2014), along with details of the instrumental setup and reduction procedure.

The Coudé Echelle Spectrograph at La Silla Observatory was used, first with the Long Camera (LC) on the 1.4 m telescope from 1992 to 1998, then with the Very Long Camera (VLC) on the 3.6 m telescope from 1998 to 2006, to collect

additional RV data on  $\epsilon$  Eridani. RV data were also collected using the HARPS spectrograph, also on the 3.6 m telescope at La Silla Observatory, during 2004–2008. Together, these data sets were published in Zechmeister et al. (2013).

### 2.2. RV Data Analysis

All new spectroscopic observations from Keck/HIRES and APF/Levy were reduced using the standard CPS pipeline (Howard et al. 2010). The iodine-free template spectrum was deconvolved with the instrumental PSF and used to forward model each observation’s relative RV. The iodine lines imprinted on the stellar spectrum by the iodine cell were used as a stable wavelength calibration, and the instrumental PSF was modeled as the sum of several Gaussians (Butler et al. 1996). Per the standard CPS RV pipeline, each spectrum was divided into approximately 700 spectral “chunks” for which the RV was individually calculated. The final RV and internal precision were calculated as the weighted average of each of these chunks. Chunks with RVs that are more consistent across observations are given higher weight. Those chunks with a larger scatter are given a lower weight. The RV observations from Keck/HIRES and APF/Levy are listed in Tables 5 and 6, respectively. These data are not offset-subtracted to account for different zero-points, and the uncertainties reported in the tables reflect the weighted standard deviations of the chunk-by-chunk RVs and do not include systematic uncertainty such as jitter.

In combination among HIRES, the APF, and the other instruments incorporated, a total of 458 high-precision RV observations have been taken, over an unprecedented time baseline of 30 yr. We note that the literature RV data included in this study were analyzed using a separate RV pipeline, which in some cases did not include a correction for the secular acceleration of the star. Secular acceleration is caused by the space motion of a star and depends on its proper motion and distance. For  $\epsilon$  Eridani, we calculate a secular acceleration signal of  $0.07 \text{ ms}^{-1} \text{ yr}^{-1}$  (Zechmeister et al. 2009). This is accounted for in the HIRES and APF data extraction, and most likely in the Lick pipeline, but is not included in the reduction for the CES and HARPS data. However, the amplitude of this effect is much smaller than the amplitude of RV variation observed in the RVs due to stellar activity and the planetary orbit. Because each of the CES and HARPS data sets cover less than 10 yr, we expect to see less than  $1 \text{ m s}^{-1}$  variation across each full data set. We tested running the analysis with and without applying these corrections. All of the resulting orbital parameters were consistent to within  $\sim 0.1\sigma$ . We therefore neglect this correction in our RV analyses. From the combined RV data set, a clear periodicity of approximately 7 yr is evident, both by eye and in a periodogram of the RV data. We assess this periodicity in Section 4.2.

$\epsilon$  Eridani’s youth results in significant stellar magnetic activity. Convection-induced motions on the stellar surface cause slight variations in the spectral line profiles, leading to variations in the inferred RV that do not reflect motion caused by a planetary companion. As a result, stellar magnetic activity may mimic the RV signal of an orbiting planet, resulting in false positives. We therefore extract  $S_{\text{HK}}$  values from each of the HIRES and APF spectra taken for  $\epsilon$  Eridani.  $S_{\text{HK}}$  is a measure of the excess emission at the cores of the Ca II H and K lines due to chromospheric activity; it correlates with stellar magnetic activity, such as spots and faculae, which might have

**Table 2**  
Observing log for NIRC2 Imaging Data

| Properties                             | Value                           | Value      | Value      |
|--|---------------------------------|------------|------------|
| UT date (yyyy mm dd)                   | 2017-01-09                      | 2017-01-10 | 2017-01-11 |
| UT start time (hh:mm:ss)               | 05:11:55                        | 05:12:47   | 05:48:08   |
| UT end time (hh:mm:ss)                 | 09:14:11                        | 09:31:09   | 08:36:14   |
| Discr. Int. Time (s)                   | 0.5                             | ...        | ...        |
| Coadds                                 | 60                              | ...        | ...        |
| Number of frames                       | 210                             | 260        | 154        |
| Total integration time (s)             | 6300                            | 7800       | 4620       |
| Plate scale (mas/pix)                  | 9.942 (“narrow”)                | ...        | ...        |
| Total FoV                              | $r \simeq 5''$ (vortex mount)   | ...        | ...        |
| Filter                                 | Ms [4.549, 4.790] $\mu\text{m}$ | ...        | ...        |
| Coronagraph                            | Vortex (AGPM)                   | ...        | ...        |
| Lyot stop                              | Inscribed circle                | ...        | ...        |
| 0.5 $\mu\text{m}$ DIMM seeing ( $''$ ) | 0.52                            | 0.64       | 0.97       |
| Par. angle start-end ( $^\circ$ )      | -36 - +52                       | -35 - +55  | -20 - +46  |

effects on the RVs extracted from the spectra (Isaacson & Fischer 2010).

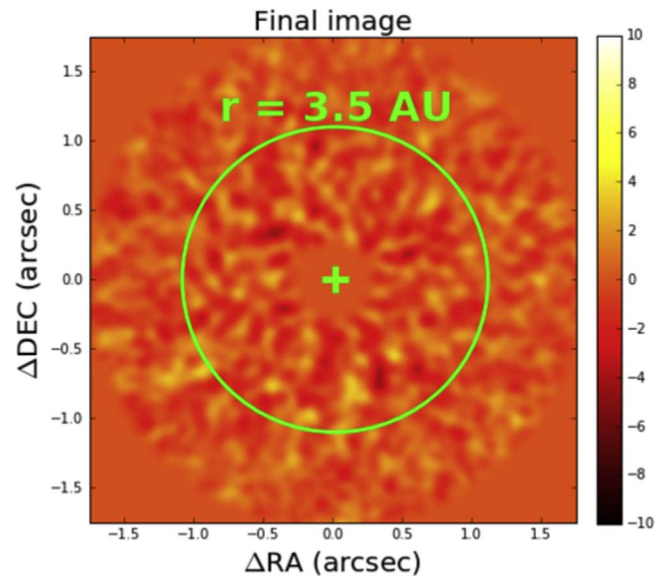
### 3. High-contrast Imaging

Here, we present our new deep, direct, high-contrast imaging observations and data analysis of  $\epsilon$  Eridani using the Keck NIRC2 vortex coronagraph.

#### 3.1. High-contrast Imaging Observations

We observed  $\epsilon$  Eridani over three consecutive nights in 2017 January (see Table 2). We used the vector vortex coronagraph installed in NIRC2 (Serabyn et al. 2017), the near-infrared camera and spectrograph behind the adaptive optics system of the 10 m Keck II telescope at W.M. Keck Observatory. The vortex coronagraph is a phase-mask coronagraph enabling high-contrast imaging at very small angles close to the diffraction limit of the 10 m Keck telescope at  $4.67 \mu\text{m}$  ( $\simeq 0''.1$ ). The starlight suppression capability of the vortex coronagraph is induced by a  $4\pi$  radian phase ramp wrapping around the optical axis. When the coherent adaptively corrected point spread function (PSF) is centered on the vortex phase singularity, the on-axis starlight is redirected outside the geometric image of the telescope pupil formed downstream from the coronagraph, where it is blocked by means of an undersized diaphragm (the Lyot stop). The vector vortex coronagraph installed in NIRC2 was made from a circularly concentric subwavelength grating etched onto a synthetic diamond substrate (Annular Groove Phase Mask coronagraph or AGPM) (Mawet et al. 2005; Vargas Catalán et al. 2016).

Median 0.5  $\mu\text{m}$  DIMM seeing conditions ranged from  $0''.52$  to  $0''.97$  (see Table 2). The adaptive optics system provided excellent correction in the  $Ms$ -band ( $[4.549, 4.790] \mu\text{m}$ ) with a Strehl ratio of about 90% (NIRC2 quicklook estimate), similar to the image quality provided at shorter wavelengths by extreme adaptive optics systems such as the Gemini Planet Imager (GPI, Macintosh et al. 2014), SPHERE (Beuzit et al. 2008), and



**Figure 1.** Final reduced image of  $\epsilon$  Eridani, using PCA, and 120 principal components in the PSF reconstruction. The scale is linear in analog to digital units (ADU).

SCEXAO (Jovanovic et al. 2015). The alignment of the star onto the coronagraph center, a key to high contrast at small angles, was performed using the quadrant analysis of coronagraphic images for tip-tilt sensing (QACITS) (Huby et al. 2015, 2017). The QACITS pointing control uses NIRC2 focal-plane coronagraphic science images in a closed feedback loop with the Keck adaptive optics tip-tilt mirror (Huby et al. 2017; Mawet et al. 2017; Serabyn et al. 2017). The typical low-frequency centering accuracy provided by QACITS is  $\simeq 0.025\lambda/D$  rms, or  $\simeq 2$  mas rms.

All of our observations were performed in vertical angle mode, which forces the AO derotator to track the telescope pupil (following the elevation angle) instead of the sky, effectively allowing the field to rotate with the parallactic angle, enabling angular differential imaging (ADI) (Marois et al. 2006).

#### 3.2. Image Post-processing

After correcting for bad pixels, flat-fielding, subtracting sky background frames using principal component analysis (PCA), and co-registering the images, we applied PCA (Soummer et al. 2012; Gomez Gonzalez et al. 2017) to estimate and subtract the post-coronagraphic residual stellar contribution from the images. We used the open-source Vortex Image Processing—VIP<sup>25</sup>—software package (Gomez Gonzalez et al. 2017), and applied PCA on the combined data from all three nights, totaling more than 5 hr of open shutter integration time (see Table 2 for details). We used a numerical mask  $2\lambda/D$  in radius to occult the bright stellar residuals close to the vortex coronagraph inner working angle.

The final image (Figure 1) was obtained by pooling all three nights together in a single data set totaling 624 frames. The PSF was reconstructed by using 120 principal components and projections on the  $351 \times 351$  pixel frames excluding the central numerical mask ( $2\lambda/D$  in radius). This number of principal components was optimized to yield the best final contrast limits in the 1–5 au region of interest, optimally trading

<sup>25</sup> <https://github.com/vortex-exoplanet/VIP>

off speckle noise and self-subtraction effects. The final image (Figure 1) does not show any particular feature and is consistent with whitened speckle noise.

#### 4. Analysis

In this section, we present our nondetection and robust detection limits from direct imaging, additional tests on the RV data, as well as our joint analysis of both data sets.

##### 4.1. Robust Detection Limits from Direct Imaging

Following Mawet et al. (2014), we assume that ADI and PCA post-processing whiten the residual noise in the final reduced image through two complementary mechanisms. First, PCA removes the correlated component of the noise by subtracting off the stellar contribution, revealing underlying independent noise processes such as background, photon Poisson noise, readout noise, and dark current. Second, the ADI frame combination provides additional whitening due to the field rotation during the observing sequence and subsequent derotation, and by virtue of the central limit theorem, regardless of the underlying distribution of the noise (Marois et al. 2006, 2008). Henceforth, we assume Gaussian statistics to describe the noise of our images. Our next task is to look for point sources, and if none are found, place meaningful upper limits. Whether or not point sources are found, we will use our data to constrain the planet mass posterior distribution as a function of projected separation.

For this task, we choose to convert flux levels into mass estimates using the COND evolutionary model (Baraffe et al. 2003) for the three ages considered in this work: 200, 400, and 800 Myr. The young age end of our bracket (200 Myr) is derived from a pure kinematic analysis (Fuhrmann 2004). The 400 and 800 Myr estimates are from Mamajek & Hillenbrand (2008), who used chromospheric activities and spin as age indicators.

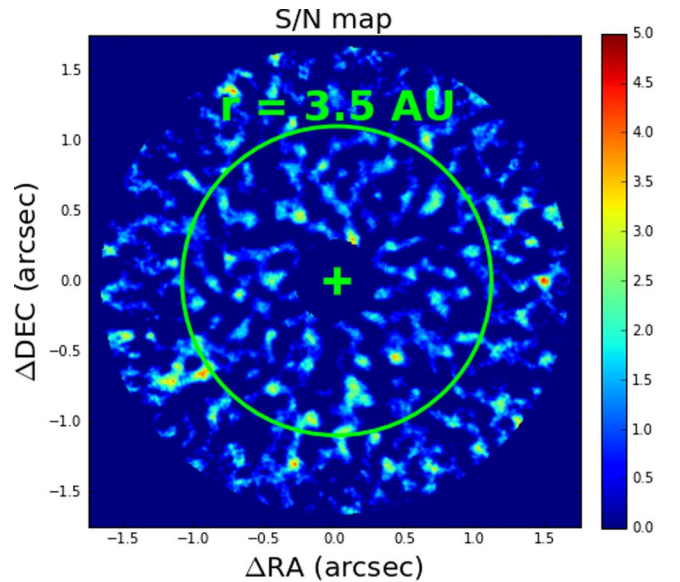
As noted by Bowler (2016), the COND model is part of the hot-start model family, which begins with arbitrarily large radii and oversimplified, idealized initial conditions. It ignores the effects of accretion and mass assembly. The COND model represents the most luminous—and thus optimistic—outcome. At the adolescent age range of  $\epsilon$  Eridani, initial conditions of the formation of a Jupiter-mass gas giant have mostly been forgotten (Marley et al. 2007; Fortney et al. 2008) and have a minor impact on mass estimates. Moreover, a very practical reason why COND was used is because it is the only model readily providing open-source tables extending into the low-mass regime  $9 < 1 M_{\text{Jup}}$  reached by our data (see Section 5.1).

##### 4.1.1. Direct Imaging Nondetection

Signal detection is a balancing act where one trades off the risk of false alarm with sensitivity. The signal detection threshold  $\tau$  is related to the risk of false alarm, or false positive fraction (FPF), as follows:

$$\text{FPF} = \frac{\text{FP}}{\text{TN} + \text{FP}} = \int_{\tau}^{+\infty} p(x|H_0) dx \quad (1)$$

where  $x$  is the intensity of the residual speckles in our images,  $p(x|H_0)$  is the probability density function of  $x$  under the null hypothesis  $H_0$ , FP is the number of false positives, and TN is the number of true negatives. Assuming Gaussian noise



**Figure 2.** S/N map for our most sensitive reduction, using 120 principal components. We used the S/N map function implemented in open source package VIP (Gomez Gonzalez et al. 2017). The method uses the annulus-wise approach presented in Mawet et al. (2014). No source is detected above  $5\sigma$ . The green circle delineates the planet’s project separation at  $\approx 3.5$  au.

statistics, the traditional  $\tau = 5\sigma$  threshold yields an FPF of  $2.98 \times 10^{-7}$ .

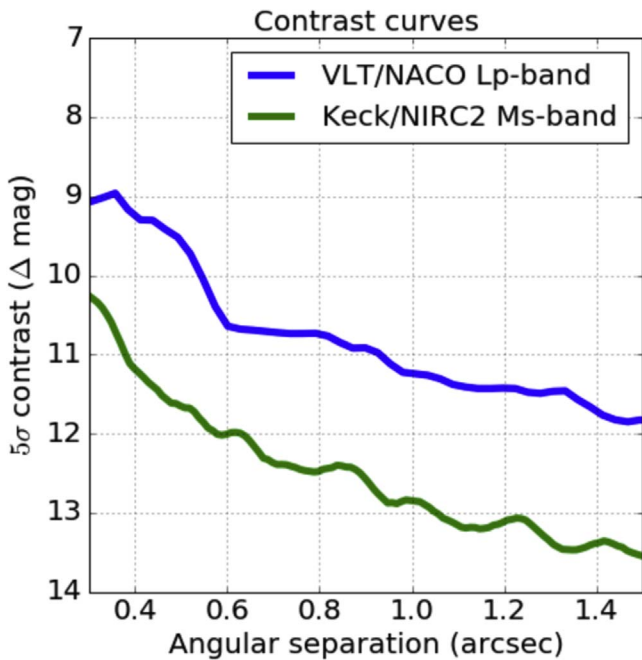
Applying the  $\tau = 5\sigma$  threshold to the S/N map generated from our most sensitive reduction, which occurs for a number of principal components equal to 120, yields no detection, consistent with a null result. In other words,  $\epsilon$  Eridani b is not detected in our deep imaging data to the  $5\sigma$  threshold. To compute the S/N map, we used the annulus-wise approach outlined in Mawet et al. (2014), and implemented in the open-source Python-based Vortex Imaging Pipeline (Gomez Gonzalez et al. 2017). The noise in an annulus at radius  $r$  (units of  $\lambda/D$ ) is computed as the standard deviation of the  $n = 2\pi r$  resolution elements at that radius. The algorithm throughput is computed using fake companion injection-recovery tests at every location in the image. This step is necessary to account for ADI self-subtraction effects. The result is shown in Figure 2.

To quantify our sensitivity, also known as “completeness,” we use the true positive fraction (TPF), defined as

$$\text{TPF} = \frac{\text{TP}}{\text{TP} + \text{FN}} = \int_{\tau}^{+\infty} p(x|H_1) dx \quad (2)$$

with  $p(x|H_1)$ , the probability density function of  $x$  under the hypothesis  $H_1$ —signal present, and where TP is the number of true positives and FN the number of false negatives. For instance, a 95% sensitivity (or completeness) for a given signal  $I$  and detection threshold  $\tau$  means that 95% of the objects at the intensity level  $I$  will statistically be recovered from the data.

The sensitivity contours, or “performance maps” (Jensen-Clem et al. 2018) for a uniform threshold corresponding to  $2.98 \times 10^{-7}$  FPF are shown in Figure 4. The choice of threshold is assuming Gaussian noise statistics and accounts for small sample statistics as in Mawet et al. (2014). At the location of the elusive RV exoplanet, the threshold corrected for small sample statistics converges to  $\tau \approx 5\sigma$ . The corresponding traditional  $\tau = 5\sigma$  contrast curve at 50% completeness is shown in Figure 3.



**Figure 3.** Traditional  $\tau = 5\sigma$  contrast curves comparing our Keck/NIRC2 vortex coronagraph *Ms*-band data to the VLT/NACO *Lp*-band data (PI: Quanz, Program ID: 090.C-0777(A)) presented in Mizuki et al. (2016) and reprocessed here with the VIP package.

#### 4.1.2. Comparison to Previous Direct Imaging Results

Mizuki et al. (2016) presented an extensive direct imaging compilation and data analysis for  $\epsilon$  Eridani. The authors analyzed data from Subaru/HiCIAO, Gemini/NICI, and VLT/NACO. Here, we focus on the deepest data set reported in Mizuki et al. (2016), which is the *Lp*-band NACO data from PI: Quanz (Program ID: 090.C-0777(A)). This non-coronagraphic ADI sequence totals 146.3 minutes of integration time and about  $67^\circ$  of parallactic angle rotation. Mizuki et al. (2016) report  $5\sigma$  and 50% completeness mass sensitivities using the hot start COND evolutionary model that are  $>10 M_J$  at 1 au for all three ages considered here, i.e., 200, 400, and 800 Myr; at 2 au, they are  $\simeq 2.5 M_J$ ,  $\simeq 4 M_J$ , and  $\simeq 6.5 M_J$ , respectively; at 3 au, they are  $\simeq 2 M_J$ ,  $\simeq 3 M_J$ , and  $\simeq 5 M_J$ , respectively.

For consistency, we reprocessed the VLT/NACO data with the VIP package and computed completeness maps using the same standards as for our Keck/NIRC2 data. The results are shown in Figure 5. Our computed  $5\sigma$  and 50% completeness mass sensitivities using the hot start COND evolutionary model for the VLT/NACO *Lp*-band data are  $>10 M_J$  at 1 au for all three ages considered here, i.e., 200, 400, and 800 Myr; at 2 au, they are  $\simeq 6.5 M_J$  at 200 Myr and  $>10 M_J$  at both 400 and 800 Myr; at 3 au, they are  $\simeq 5.5 M_J$ ,  $\simeq 8 M_J$ , and  $>10 M_J$ , respectively.

Our computed  $5\sigma$  and 50% completeness results for the VLT/NACO *Lp*-band data are systematically worse than those presented in Mizuki et al. (2016). We note a discrepancy in mass between the published results and our values, by a factor of two. We suggest that it may be the result of inaccurate flux loss calibrations in Mizuki et al. (2016), which is a common occurrence with ADI data sets.

We find that our *Ms*-band Keck/NIRC2 coronagraphic data is about a factor of 5–10 more sensitive in mass, across the range of solar system scales probed in this work, than the previous best available data set. Our  $5\sigma$  and 50% completeness

mass sensitivities using the hot start COND evolutionary model are  $\simeq 3 M_J$ ,  $\simeq 4.5 M_J$ , and  $\simeq 6.5 M_J$  at 1 au for all three ages considered here, i.e., 200, 400, and 800 Myr, respectively; at 2 au, they are  $\simeq 1.5 M_J$ ,  $\simeq 1.7 M_J$ , and  $\simeq 2.5 M_J$ , respectively; at 3 au, they are  $\simeq 0.8 M_J$ ,  $\simeq 1.7 M_J$ , and  $\simeq 5 M_J$ , respectively.

These results demonstrate the power of ground-based *Ms*-band small-angle coronagraphic imaging for nearby adolescent systems. When giant exoplanets cool down to below 1000 K, the peak of their blackbody emission shifts to 3–5  $\mu\text{m}$  mid-infrared wavelengths. Moreover, due to the  $t^{-5/4}$  dependence of bolometric luminosity on age (Stevenson 1991), mid-infrared luminosity stays relatively constant for hundreds of millions of years.

#### 4.2. Tests on the RV Data

In light of our nondetection of a planet in the NIRC2 high-contrast imaging, we consider the possibilities that the planet is not real or that the periodicity is caused by stellar activity. We utilize the RV analysis package *RadVel*<sup>26</sup> (Fulton et al. 2018) to perform a series of tests to determine the significance of the periodicity and attempt to rule out stellar activity as its source. We also test whether rotationally modulated noise must be considered in our analysis, and search for additional planets in the RV data set.

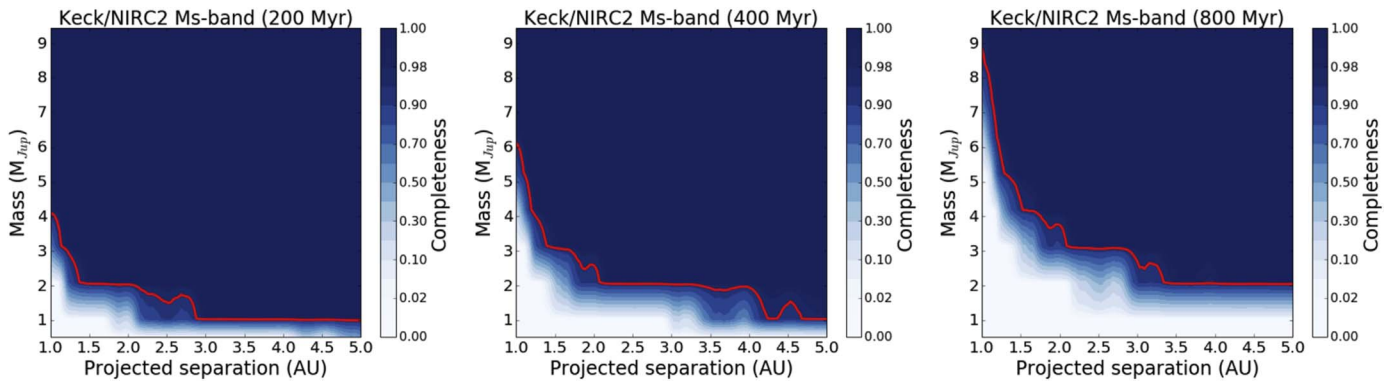
##### 4.2.1. Significance of the 7 yr Periodicity

First, we perform a one-planet fit to the RV data using *RadVel*, and compare this model to the null hypothesis of no Keplerian orbit using the Bayesian Information Criterion (BIC) to determine the significance of the 7 yr periodicity. The results of the *RadVel* MCMC analysis are located in Table 3, where  $P_b$  is the planetary orbital period,  $T_{\text{conj}_b}$  is the time of conjunction,  $e_b$  is the planetary eccentricity,  $\omega_b$  is the argument of periastron of the planet, and  $K_b$  is the Keplerian semi-amplitude.  $\gamma$  terms refer to the zero-point RV offset for each instrument, and  $\sigma$  terms are the jitter, added in quadrature to the measurement uncertainties as described in Section 2.2. The maximum likelihood solution from the *RadVel* fit is plotted in Figure 6 against the full RV data set.

For the fit, the orbit is parameterized with  $e_b$ ,  $\omega_b$ ,  $K_b$ ,  $P_b$ , and  $T_{\text{conj}_b}$ , as well as RV offsets ( $\gamma$ ) and jitter ( $\sigma$ ) terms for each instrument. Due to the periodic upgrades of the Lick/Hamilton instrument and dewar, we split the Fischer et al. (2014) Lick data into four data sets, each with its own  $\gamma$  and jitter  $\sigma$  parameter. This is warranted because Fischer et al. (2014) demonstrated that statistically significant offsets could be measured across the four upgrades in time series data on standard stars. The largest zero-point offset they measured was a  $13 \text{ m s}^{-1}$  offset between the third and fourth data set. Although these offsets should have been subtracted before the Lick/Hamilton data were published, the relative shifts between our derived  $\gamma$  parameters match well with those reported in Fischer et al. (2014) for each upgrade, implying that the offsets were not subtracted for  $\epsilon$  Eridani.

We find that the best-fit period is  $7.37 \pm 0.08 \text{ yr}$ , and that this periodicity is indeed highly significant, with  $\Delta\text{BIC} = 245.98$  between the one-planet model and the null hypothesis of no planets. Additionally, a model with fixed zero eccentricity

<sup>26</sup> Documentation available at <http://radvel.readthedocs.io/en/latest/>.



**Figure 4.** Keck/NIRC2 *Ms*-band performance/completeness maps for a  $\tau = 5\sigma$  detection threshold for all three different ages considered here. The red curve highlights the 95% completeness contour.

is preferred ( $\Delta\text{BIC} = 8.5$ ) over one with a modeled eccentricity.

#### 4.2.2. Source of the 7 yr Periodicity

We next assess whether it might be possible that the source of the periodicity at 7.37 yr is due to stellar activity, rather than a true planet.

To probe the potential effects of the magnetic activity on the RV periodicities, we examined time series data of the RVs along with the  $S_{\text{HK}}$  values from Lick, Keck, and the APF. RV and  $S_{\text{HK}}$  time series and Lomb Scargle periodograms are plotted in Figure 7.

A clear periodicity of 7.32 yr dominates the periodogram of the RV data set. This is within the  $1\sigma$  credible interval of the best-fit periodicity found with *RadVel*, which yielded a  $\Delta\text{BIC} > 200$  when we tested its significance. Once the best-fit Keplerian planetary orbit from *RadVel* is subtracted from the RV data, the residuals and their periodogram are plotted in panels (2a) and (2b) of Figure 7. The peak periodicity observed in the periodogram of the RV residuals is located at approximately 3 yr, coincident with the periodicity of the  $S_{\text{HK}}$  time series.

For the  $S_{\text{HK}}$  time series, we detect clear  $S_{\text{HK}}$  periodicities near 3 yr, indicative of a  $\sim 3$  yr magnetic activity cycle (panels (4)–(5b)). We note that the peak  $S_{\text{HK}}$  periodicity appears to be slightly discrepant between the Keck and APF data sets ( $P_{\text{Keck}} = 3.17$  yr;  $P_{\text{APF}} = 2.59$  yr), but consistent within the FWHM of the periodogram peaks. This discrepancy likely results from a variety of causes, including the shorter time baseline of the APF data, which covers only a single  $S_{\text{HK}}$  cycle, and the typically non-sinusoidal and quasiperiodic nature of stellar activity cycles. The data sets also show a small offset in the median  $S_{\text{HK}}$  value, likely due to differing calibrations between the instrumental and telescope setups. However, the amplitude of the  $S_{\text{HK}}$  variations appears consistent between the data sets.

We next test whether the 3 yr activity cycle could be responsible for contributing power to the 7 yr periodicity. The longer period is not an alias of the 3 yr activity cycle, nor is it in a low-order integer ratio with the magnetic activity cycle. We perform a Keplerian fit to the RV time series from HIRES and the APF, with a period constrained at the stellar activity period (1147 days). We find an RV semi-amplitude of  $K = 4.8^{+2.2}_{-1.7}$  m s $^{-1}$  and a large eccentricity of  $0.53^{+0.24}_{-0.27}$  fits the data set best. We then subtract this fit from the RV data to determine whether removal of the activity-induced RV periodicity affects

the significance of the planet periodicity. The 7 yr periodicity in the residuals is still clearly visible by eye, and a one-planet fit to the RV residuals after the activity cycle is subtracted yields a  $\Delta\text{BIC} = 197.4$  when compared to a model with no planet.

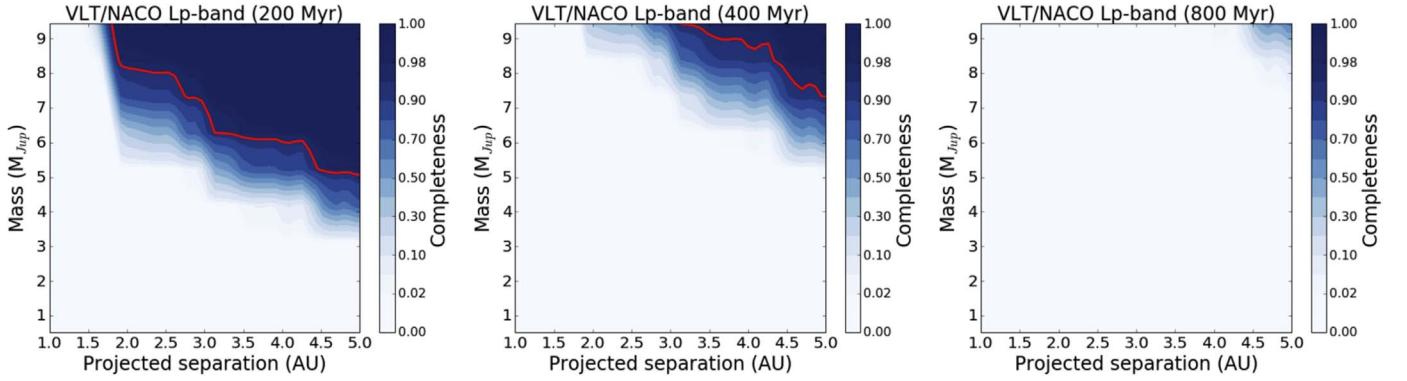
We next checked the RVs for correlation with  $S_{\text{HK}}$ . Minor correlation was detected for the Keck/HIRES data set, with a Spearman correlation coefficient of  $r_s = 0.28$  at moderate statistical significance ( $p = 0.01$ ). For the APF data set, a stronger and statistically significant correlation was found ( $r_s = 0.50$ ,  $p \ll 0.01$ ) between  $S_{\text{HK}}$  and RV. However, given that the 3 yr magnetic cycle shows up in the RV residuals, it is not surprising that RV and  $S_{\text{HK}}$  might be correlated. There is also rotationally modulated noise that might be present in both data sets near the  $\sim 11$  day rotation timescale, increasing the correlation. We attempt to determine whether the measured correlation derives from the 3 yr periodicity in both data sets, or whether it is produced by other equivalent periodicities in the RV and  $S_{\text{HK}}$  data sets.

To test this, we first performed a Keplerian fit with a period of approximately 3 yr to the Keck and APF  $S_{\text{HK}}$  time series using *RadVel*. Although stellar activity is not the same as orbital motion, we used the Keplerian function as a proxy for the long-term stellar activity cycle of  $\epsilon$  Eridani. We found a maximum probability period of  $1194^{+30}_{-25}$  days for the HIRES data and  $989^{+40}_{-26}$  days for the APF data. These periodicities are indeed discrepant by more than  $5\sigma$ . When combined, we found a period of  $1147^{+22}_{-20}$  days for the full HIRES and APF data set.

We then subtracted the maximum probability 3 yr fit from each  $S_{\text{HK}}$  data set, and examined the residual values. We found that the correlation between these  $S_{\text{HK}}$  residuals and the RV data was significantly reduced for the APF data, with  $r_s = 0.17$  and  $p = 0.04$ . This suggests that the strong correlation we detected was primarily a result of the 3 yr periodicity. For the HIRES data set, the moderately significant correlation of  $r_s = 0.28$  was unchanged.

A Lomb–Scargle periodogram of the  $S_{\text{HK}}$  residuals is displayed in Figure 8. It shows no significant peak or power near the posterior planet period at 2691 days, demonstrating that the  $S_{\text{HK}}$  time series has no significant periodicity at the planet’s orbital period.

Our next tests involved modifying our one-planet fits to the RV data to account for the stellar activity cycle in two ways. We first performed a one-planet fit to the RVs using a linear decorrelation against the  $S_{\text{HK}}$  values for the HIRES and APF data sets. We then performed a two-Keplerian fit to the RV data, in order to simultaneously characterize both the planetary



**Figure 5.** Performance/completeness maps for a  $\tau = 5\sigma$  detection threshold for all three different ages considered here using VLT/NACO *Lp*-band data (PI: Quanz, Program ID: 090.C-0777(A)) presented in Mizuki et al. (2016). The red curve highlights the 95% completeness contour.

**Table 3**  
RadVel MCMC Posteriors

| Parameter                 | Credible Interval         | Maximum Likelihood | Units                           |
|---------------------------|---------------------------|--------------------|---------------------------------|
| $P_b$                     | $2691^{+29}_{-28}$        | 2692               | days                            |
| $T_{\text{conj}b}$        | $2530054^{+800}_{-770}$   | 2530054            | JD                              |
| $e_b$                     | $0.071^{+0.061}_{-0.049}$ | 0.062              |                                 |
| $\omega_b$                | $3.13^{+0.82}_{-0.79}$    | 3.1                | radians                         |
| $K_b$                     | $11.48 \pm 0.66$          | 11.49              | $\text{m s}^{-1}$               |
| $\gamma_{\text{HIRES}}$   | $2.0 \pm 0.89$            | 2.05               | $\text{m s}^{-1}$               |
| $\gamma_{\text{HARPS}}$   | $-4.6 \pm 1.6$            | -4.8               | $\text{m s}^{-1}$               |
| $\gamma_{\text{APF}}$     | $-3 \pm 1$                | -3                 | $\text{m s}^{-1}$               |
| $\gamma_{\text{Lick}_4}$  | $-2.45^{+0.99}_{-0.96}$   | -2.41              | $\text{m s}^{-1}$               |
| $\gamma_{\text{Lick}_3}$  | $10.5^{+2.0}_{-1.9}$      | 11.0               | $\text{m s}^{-1}$               |
| $\gamma_{\text{Lick}_2}$  | $8.6 \pm 2.3$             | 8.6                | $\text{m s}^{-1}$               |
| $\gamma_{\text{Lick}_1}$  | $8.5 \pm 2.5$             | 8.5                | $\text{m s}^{-1}$               |
| $\gamma_{\text{CES+LC}}$  | $6.7 \pm 2.7$             | 6.7                | $\text{m s}^{-1}$               |
| $\gamma_{\text{CES+VLC}}$ | $3.2 \pm 1.8$             | 3.3                | $\text{m s}^{-1}$               |
| $\dot{\gamma}$            | $\equiv 0.0$              | $\equiv 0.0$       | $\text{m s}^{-1} \text{d}^{-1}$ |
| $\ddot{\gamma}$           | $\equiv 0.0$              | $\equiv 0.0$       | $\text{m s}^{-1} \text{d}^{-2}$ |
| $\sigma_{\text{HIRES}}$   | $5.99^{+0.88}_{-0.82}$    | 5.83               | $\text{m s}^{-1}$               |
| $\sigma_{\text{HARPS}}$   | $5.3^{+1.7}_{-1.6}$       | 4.8                | $\text{m s}^{-1}$               |
| $\sigma_{\text{APF}}$     | $5.26^{+0.75}_{-0.72}$    | 5.12               | $\text{m s}^{-1}$               |
| $\sigma_{\text{Lick}_4}$  | $7.1^{+0.96}_{-0.88}$     | 6.85               | $\text{m s}^{-1}$               |
| $\sigma_{\text{Lick}_3}$  | $7.6^{+1.7}_{-1.5}$       | 7.2                | $\text{m s}^{-1}$               |
| $\sigma_{\text{Lick}_2}$  | $2.8^{+2.3}_{-1.6}$       | 0.0                | $\text{m s}^{-1}$               |
| $\sigma_{\text{Lick}_1}$  | $14.5^{+2.4}_{-2.1}$      | 13.9               | $\text{m s}^{-1}$               |
| $\sigma_{\text{CES+LC}}$  | $9.8^{+3.0}_{-2.7}$       | 9.0                | $\text{m s}^{-1}$               |
| $\sigma_{\text{CES+VLC}}$ | $4.4^{+2.2}_{-2.1}$       | 3.6                | $\text{m s}^{-1}$               |

**Note.** 860,000 links saved.

Reference epoch for  $\gamma$ ,  $\dot{\gamma}$ ,  $\ddot{\gamma}$ : 2452438.84422.

orbit and the stellar activity cycle. In both cases, we checked for significant changes to the planetary orbital parameters due to accounting for the stellar activity cycle in the fit. For both tests, we find that the maximum likelihood values of the planet’s orbital parameters all agree within  $1\sigma$  credible intervals with the single-planet fit.

We note that, from the two-Keplerian fit, the best-fit second Keplerian provides some information about the stellar activity cycle. It has a best-fit period of 1079 days, or 2.95 yr, shorter than the periodicity derived from a fit to the HIRES and APF  $S_{\text{HK}}$  time series. However, though the other parameters in this fit seem to be converged, the period and time of conjunction of

the second Keplerian are clearly not converged over the iterations completed for this model. Increasing the number of iterations does not appear to improve convergence. This again points to the quasiperiodic nature of stellar activity cycles, and the different time baselines of the full RV data set and the  $S_{\text{HK}}$  time series available. The fit has an RV semi-amplitude of  $K_{\text{activity}} = 4.4 \text{ m s}^{-1}$ , lower than the semi-amplitude of the planet at  $K_b = 11.81 \pm 0.65 \text{ m s}^{-1}$ .

#### 4.2.3. Search for Additional RV Planets

We used the automated planet search algorithm described by Howard & Fulton (2016) to determine whether additional planet signatures are present in the combined RV data set. The residuals to the two-Keplerian fit were examined for additional periodic signatures. The search was performed using a 2D Keplerian Lomb–Scargle periodogram (2DKLS) (O’Toole et al. 2009).

The residuals to the two-Keplerian fit show several small peaks, but none with empirical false alarm probabilities (eFAP) (Howard & Fulton 2016) less than 1% (Figure 7, panel (3b)). A broad forest of peaks at approximately 12 days corresponds to the stellar rotation period and is likely due to spot-modulated stellar jitter. The next most significant peak is located at 108.3 days. We attempted a three-Keplerian fit to the RVs with the third Keplerian initiated at 108.3 days. However, we were unable to achieve convergence in a reasonable number of iterations, and the walkers were poorly behaved. This serves as evidence against the inclusion of a third periodicity. We conclude that there is insufficient evidence to suggest an inner planet to  $\epsilon$  Eridani b exists.

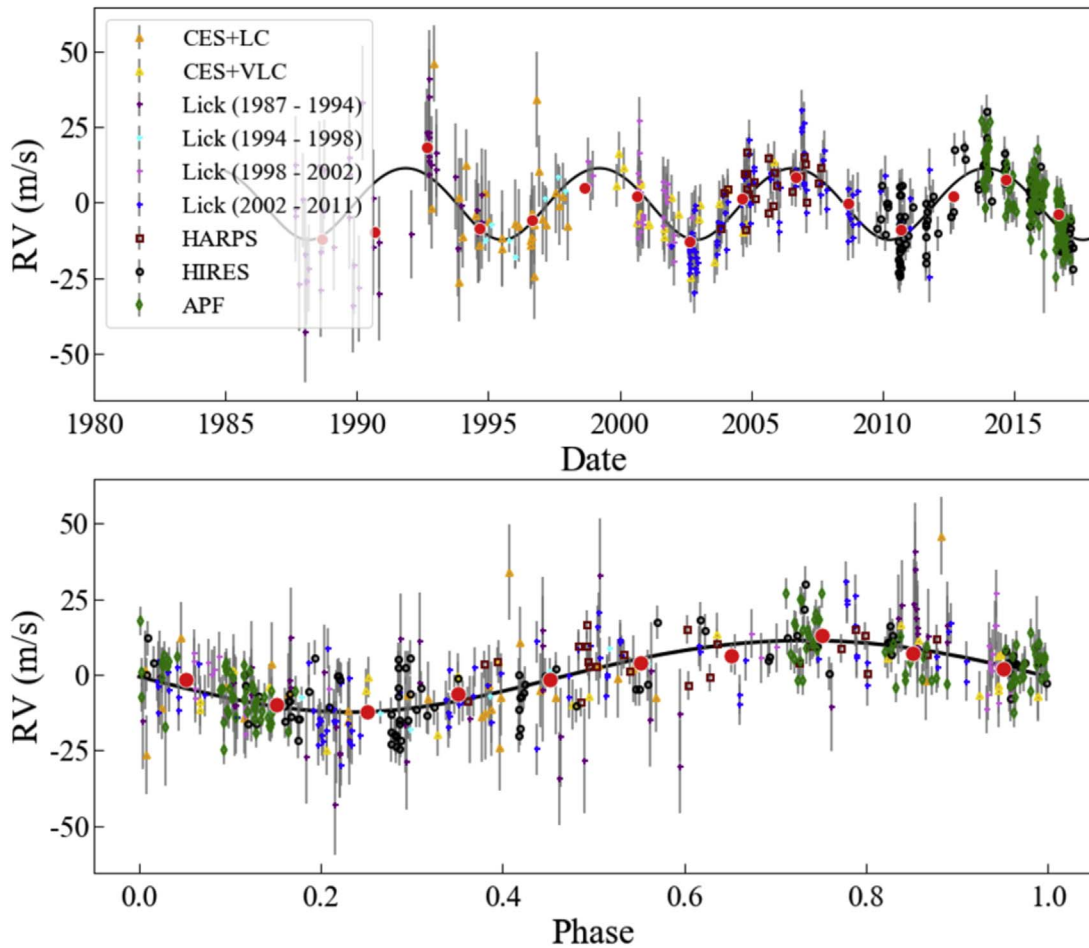
RV and residual time series, as well as 2DKLS periodograms used for the additional planet search, are plotted in Figure 7, panel (3a) and (3b).

#### 4.2.4. Gaussian Processes Fits

For all of these analyses, we have assumed white noise and added a “jitter” term in quadrature to account for uncertainty due to stellar activity. We assessed whether this was reasonable by performing a one-planet fit using RadVel and including a Gaussian processes model to account for rotationally modulated stellar noise (S. Blunt & A. W. Howard 2018, in preparation; M. Kosiarek et al. 2018, in preparation) as well as the 3 yr stellar activity cycle.

First, we used RadVel with a new implementation of GP regression using the quasiperiodic covariance kernel to fit four





**Figure 6.** Time series and phase-folded radial velocity curves from all data sets are plotted. The maximum probability single-Keplerian model from `RadVel` is overlotted, as are the binned data (red). The plotted error bars include the internal rms derived from the RV code, as well as the fitted stellar and instrumental jitter parameter  $\sigma_j$  for each instrument.

GP hyperparameters in addition to the Keplerian parameters for a single planet and a white noise term  $\sigma_j$ . The hyperparameters for the quasiperiodic kernel are the amplitude of the covariance function ( $h$ ); the period of the correlated noise ( $\theta$ , in this case trained on the rotation period of the star); the characteristic decay timescale of the correlation ( $\lambda$ , a proxy for the typical spot lifetime); and the coherence scale ( $w$ , sometimes called the structure parameter) (Grunblatt et al. 2015; López-Morales et al. 2016).

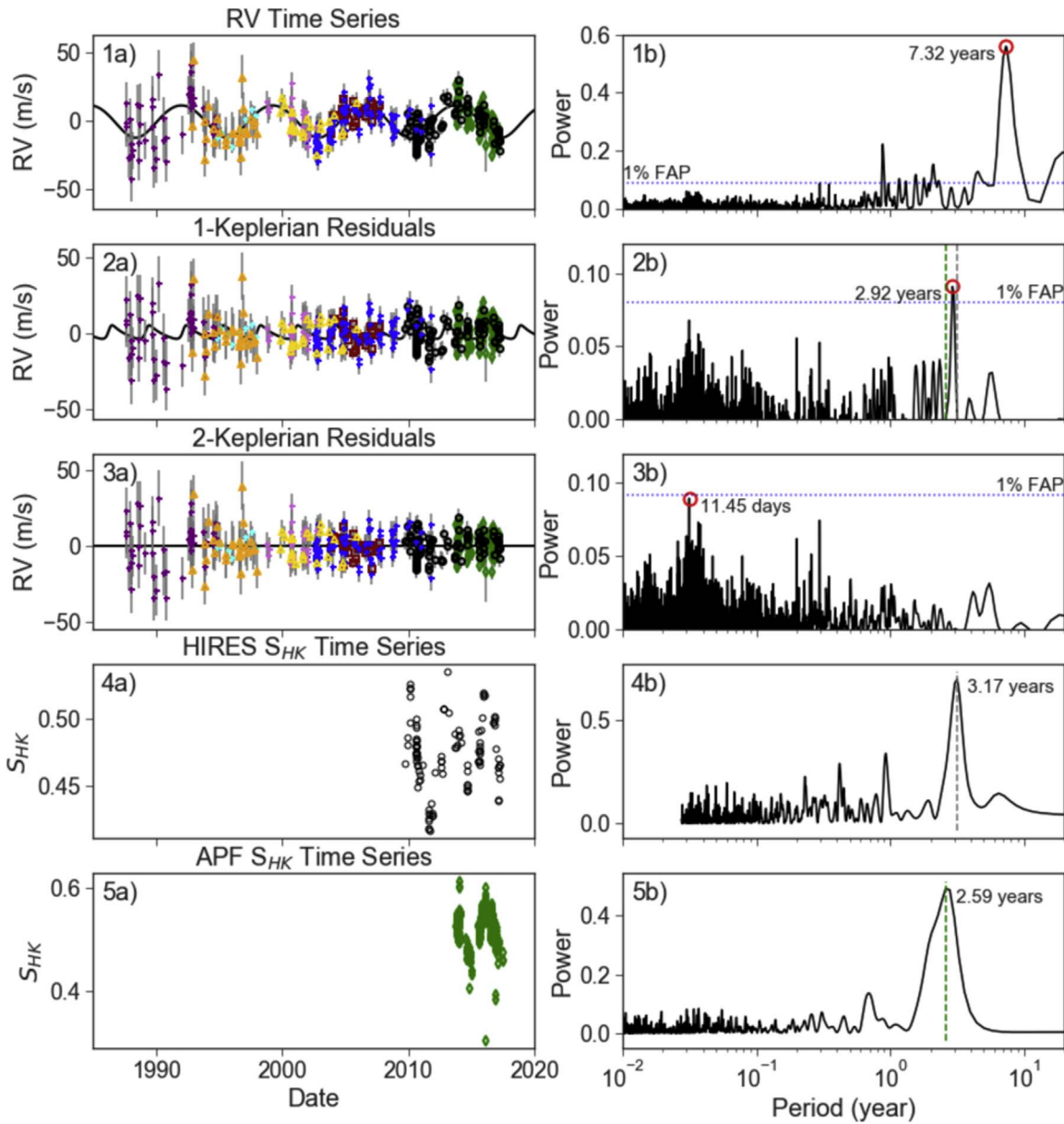
We applied a Gaussian prior to the rotation period of  $\theta = 11.45 \pm 2.0$  days, based on the periodicity observed in the RV residuals to the two-Keplerian fit, but sufficiently wide to allow the model flexibility. The covariance amplitudes  $h$  for each instrument were constrained with a Jeffrey’s prior truncated at 0.1 and 100  $\text{m s}^{-1}$ . We imposed a uniform prior of 0–1 yr on the exponential decay timescale parameter  $\lambda$ . We chose a Gaussian prior for  $w$  of  $0.5 \pm 0.05$ , following López-Morales et al. (2016).

The results of our GP analysis provide constraints on the hyperparameters, indicating that the rotation period is  $11.64^{+0.33}_{-0.24}$  days and the exponential decay timescale is  $49^{+15}_{-11}$  days. The amplitude parameters for each instrument ranged from 0.0 to 13.4  $\text{m s}^{-1}$ , and were highest for the earliest Lick RV data. For some of the data sets, the cadence of the observations likely reduced their sensitivity

to correlated noise on the rotation timescale, resulting in GP amplitudes consistent with zero. For other instruments, notably the HIRES and APF data, the white noise jitter term  $\sigma_j$  was significantly reduced in the GP model, compared with the standard RV solution.

However, when comparing the derived properties of the planet, we find that the GP analysis has no noticeable effect on the planet’s orbital parameters. The period, RV semi-amplitude, eccentricity, time of conjunction, and argument of periastron constraints from the GP regression analysis all agree within  $1\sigma$  with the values derived from the traditional one-planet fit. We therefore conclude that the rotationally modulated noise does not significantly affect the planet’s orbital parameters.

We additionally performed a one-planet fit using GP regression to model the 3 yr stellar activity cycle. For this test case, we used a periodic GP kernel because each data set covers only a relatively few cycles of the stellar activity cycle. Unlike activity signatures at the stellar rotation period, we do not expect to see significant decay or decorrelation of the 3 yr cycle over the time span of our data set. This periodic GP model had hyperparameters describing the periodicity ( $\theta$ ), amplitude ( $h$ ), and structure parameter ( $w$ ), but no exponential decay. This analysis is somewhat akin to our two-Keplerian fit, but allows more flexibility to fit the noise than a Keplerian. For this model,

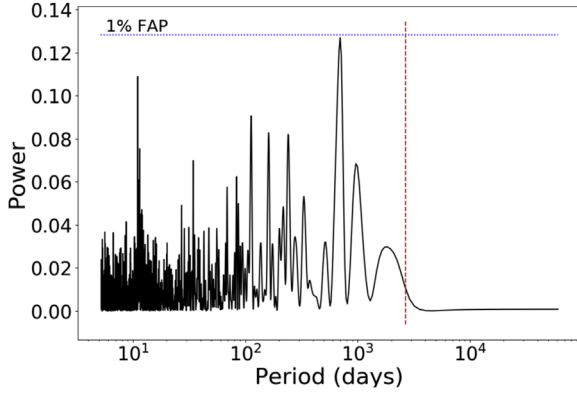


**Figure 7.** Time series (a) and Lomb–Scargle periodograms (b). Panels (1)–(3) show the periodicities of the radial velocity measurements, residuals to a one-Keplerian (planet)  $\text{RadVel}$  fit, and residuals to a two-Keplerian (planet + stellar activity)  $\text{RadVel}$  fit, respectively. Panels (4) and (5) show the time series and periodograms of the Keck and APF  $S_{HK}$  values. The peak periodicities for each data set are indicated in the periodogram plots. The periodicities of the  $S_{HK}$  data sets (panels 4–5) are overplotted in the second periodogram panel (2b), showing the correspondence between  $S_{HK}$  periodicity and the secondary, activity-induced peak in the RV residuals. The broad, low-significance peak at 11.45 days in panel (3b) corresponds to the stellar rotation period. Plotting symbols for the RV data sets are the same as in Figure 6.

we placed a Gaussian prior of  $\theta = 1147 \pm 20$  days on the GP period parameter, based on the Keplerian fit to the  $S_{HK}$  values. We found that, when allowing each instrument its own GP amplitude parameter,  $h$ , nearly all of the instrumental amplitudes were best fit with values very close to zero, so instead we fit for only a single GP amplitude across all instrumental data sets. We constrained this parameter with a Jeffreys prior bounded at  $0.01\text{--}100 \text{ m s}^{-1}$ . We again used the  $w = 0.5 \pm 0.05$  prior for the structure parameter, after testing out fits at several values between 0 and 1. It remains unclear whether this was the optimal choice, given that the physical interpretation of this parameter would be different for the long-term stellar activity cycle as compared with the rotationally modulated spot noise.

The results of this analysis indicate a GP periodicity of  $\theta = 1149 \pm 17$  days, a slightly tighter constraint than the imposed prior. The GP amplitude parameter was constrained to be  $h = 4.26_{-1.01}^{+1.21} \text{ m s}^{-1}$ , comparable with the posteriors for the RV semi-amplitude of the second Keplerian in the two-Keplerian fit. Importantly, the model posteriors on the planetary parameters were again consistent within  $1\sigma$  with our traditional one-planet fit for all parameters, including the white noise jitter terms  $\sigma_j$  as well as the orbital period, RV semi-amplitude, eccentricity, and Keplerian angles.

We note that the traditional one-planet fit is preferred over the one-planet Gaussian processes fit by  $\Delta\text{BIC} = 19.7$ . The two-Keplerian fit is also preferred over the GP one-planet



**Figure 8.** Periodogram of the HIRES and APF  $S_{\text{HK}}$  residuals to the  $\sim 3$  year fit. The red dotted line shows the best-fit period of the planet from our initial one-planet fit. Like the  $S_{\text{HK}}$  periodograms shown in Figure 7 panels (4)–(5b), there is no power at the planet’s orbital period. Even when the peak periodicity is removed for each data set, no additional power appears at the planet’s 7.37 year orbital period. This indicates that stellar activity is not likely to cause the 7.37 year periodicity in the radial velocity data.

model, with  $\Delta\text{BIC} = 30.6$ , despite having two additional free parameters and nominally less flexibility than the GP model.

These tests demonstrate that the addition of a Keplerian or Gaussian-process model to account for stellar activity (both rotationally modulated activity and the long-period stellar activity cycle) does not strongly influence the results of the planetary orbital fit. The GP fit in particular was statistically disfavored compared to the simpler Keplerian model based on  $\Delta\text{BIC}$ . We therefore choose to restrict our subsequent analyses to consider only a single planet and only white noise. Going forward, the uncertainty due to stellar activity is added in quadrature as a white-noise “jitter” term and red noise is not considered.

#### 4.3. Combining Constraints from Imaging and RV

By combining the imaging and RV data sets, it is possible to place tighter upper limits on the mass of the companion. Indeed, the RV data provides a lower limit on the planet mass ( $M \sin i$ ), while the direct imaging data complements it with an upper limit.

An MCMC will be used to infer the posterior on the masses and orbital parameters of the system, noted as  $\Theta$ . The noise in the RV measurements  $d_{\text{RV}}$  and in the images  $d_{\text{DI}}$  is independent, which means that the joint likelihood is thus separable:

$$\mathcal{P}(d_{\text{DI}}, d_{\text{RV}}|\Theta) = \mathcal{P}(d_{\text{RV}}|\Theta)\mathcal{P}(d_{\text{DI}}|\Theta). \quad (3)$$

##### 4.3.1. Direct Imaging Likelihood

In this section, we detail the computation of the direct imaging likelihood (Ruffio et al. 2018). The direct imaging data  $d_{\text{DI}}$ , temporarily shortened to  $d$ , is a vector of  $N_{\text{exp}} \times N_{\text{pix}}$  elements where  $N_{\text{exp}}$  is the number of exposures in the data set and  $N_{\text{pix}}$  the number of pixels in an image. It is the concatenation of all the vectorized speckle subtracted single exposures. A point source is defined from its position  $x$  and its brightness  $i$ . We also define  $n$  as a Gaussian random vector with zero mean and covariance matrix  $\Sigma$ . We assume that the

noise is uncorrelated and that  $\Sigma$  is therefore diagonal

$$d = im + n \quad (4)$$

with  $m = m(x)$  being a normalized planet model at the position  $x$ .

Assuming Gaussian noise, the direct imaging likelihood is given by:

$$\begin{aligned} \mathcal{P}(d|i, x) &= \frac{1}{\sqrt{2\pi|\Sigma|}} \exp\left\{-\frac{1}{2}(d - im)^\top \Sigma^{-1}(d - im)\right\} \\ &\propto \exp\left\{-\frac{1}{2}(i^2 m^\top \Sigma^{-1} m - 2id^\top \Sigma^{-1} m)\right\}. \end{aligned} \quad (5)$$

We have used the fact that  $d^\top \Sigma^{-1} d$  is a constant because we are not inferring the direct imaging covariance.

The estimated brightness  $\tilde{i}_x$ , in a maximum likelihood sense, and associated error bar  $\sigma_x$  are defined as:

$$\tilde{i}_x = \frac{d^\top \Sigma^{-1} m}{m^\top \Sigma^{-1} m}, \quad (6)$$

and

$$\sigma_x^2 = (m^\top \Sigma^{-1} m)^{-1}. \quad (7)$$

We can therefore rewrite the logarithm of the direct imaging likelihood as a function of these quantities (Ruffio et al. 2018),

$$\log \mathcal{P}(d|i, x) = -\frac{1}{2\sigma_x^2}(i^2 - 2i\tilde{i}_x). \quad (8)$$

The definition of the planet model  $m$  is challenging when using a PCA-based image processing. Indeed, while it subtracts the speckle pattern, it also distorts the signal of the planet. The distortion is generally not accounted for in a classical data reduction such as the one used in Section 4.1, which is why it is more convenient to adopt a Forward Model Matched Filter (FMMF) approach as described in Ruffio et al. (2017). The FMMF computes the map of estimated brightness and standard deviation used in Equation (8) by deriving a linear approximation of the distorted planet signal for each independent exposure, called the forward model (Pueyo 2016).

We showed that the likelihood can theoretically be calculated directly from the final products of the FMMF. In practice, the noise is correlated and not perfectly Gaussian, resulting in the standard deviation being underestimated and possibly biasing the estimated brightness. We therefore recalibrate the S/N by dividing it by its standard deviation computed in concentric annuli. The estimated brightness map is corrected for algorithm throughput using simulated planet injection and recovery. The likelihood is computed for the fully calibrated S/N maps.

FMMF is part of a Python implementation of the PCA algorithm presented in Soummer et al. (2012) called `PyKLIP`<sup>27</sup> (Wang et al. 2015). The principal components for each exposure are calculated from a reference library of the 200 most correlated images from which only the first 20 modes are kept. Images in which the planet would be overlapping with the current exposure are not considered to be part of the reference library, to limit the self- and over-subtraction using an exclusion criterion of seven pixels ( $0.7\lambda/D$ ). The speckle

<sup>27</sup> Available under open-source license at <https://bitbucket.org/pyklip/pyklip>.

subtraction is independently performed on small sectors of the image.

#### 4.3.2. Joint Likelihood and Priors

We implement a Markov-chain Monte Carlo analysis of the combined RV data from the Coudé Echelle Spectrograph, HARPS, Lick/Hamilton, Keck/HIRES, and APF/Levy instruments, as well as the single-epoch direct imaging data. We solve for the full Keplerian orbital parameters, including orbital inclination and longitude of the ascending node, which are not typically included in RV-only orbital analyses. Including the full Keplerian parameters allows us to calculate the projected position of the companion at the imaging epoch for each model orbit. This is necessary to calculate an additional likelihood based on the direct imaging data.

The full log-likelihood function used for this analysis is:

$$\log \mathcal{P}(d_{\text{DI}}, d_{\text{RV}} | \Theta) = -\frac{1}{2\sigma_x^2} (i^2 - 2i\tilde{i}_x) - \sum_i \left[ \frac{(v_i - v_m(t_i))^2}{2(\sigma_i^2 + \sigma_j^2)} + \log \sqrt{2\pi(\sigma_i^2 + \sigma_j^2)} \right]. \quad (9)$$

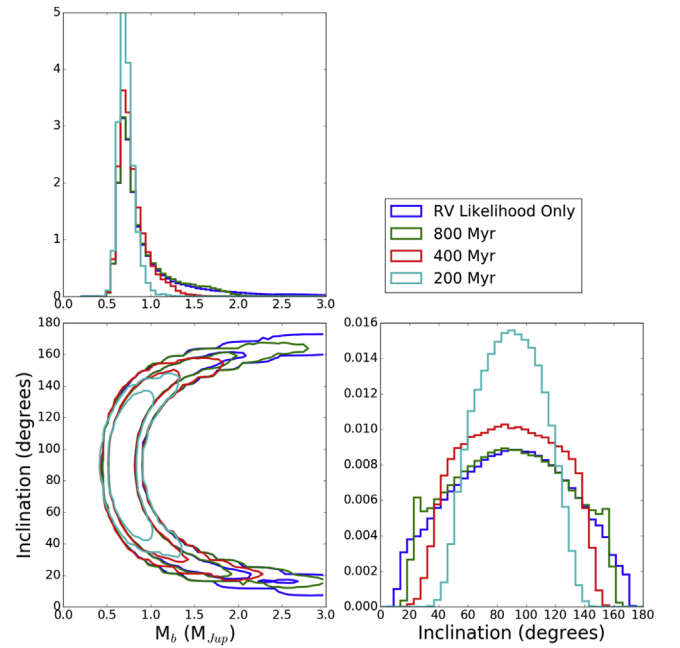
The RV component of the likelihood comes from (Howard et al. 2014). Here,  $v_i = v_{i,\text{inst}} - \gamma_{\text{inst}}$  is the offset-subtracted RV measurement;  $\sigma_i$  refers to the internal uncertainty for each measurement;  $v_m(t_i)$  is the Keplerian model velocity at the time of each observation; and  $\sigma_j$  is the instrument-specific jitter term, which contributes additional uncertainty due to both stellar activity and instrumental noise. In these models, each instrument’s RV offset ( $\gamma_{\text{inst}}$ ) and jitter term ( $\sigma_{j,\text{inst}}$ ) are included as free parameters in the fit. A description of the direct imaging component of the likelihood is available in Section 4.3.1.

We draw from uniform distributions in  $\log P$ ,  $\log M_b$ ,  $\cos i$ ,  $\sqrt{e} \cos \omega$ ,  $\sqrt{e} \sin \omega$ ,  $\Omega$ , mean anomaly at the epoch of the first observation, and  $\gamma_{\text{inst}}$ .

We place a tight Gaussian prior of  $M_* = 0.781 \pm 0.078 M_\odot$  on the primary stellar mass, based on the interferometric results of Boyajian et al. (2012). Other groups have measured slightly different but generally consistent stellar masses for  $\epsilon$  Eridani. Valenti & Fischer (2005) report a spectroscopic mass of  $M_* = 0.708 \pm 0.067 M_\odot$ ; Takeda et al. (2007) report a discrepant spectroscopic result of  $M_* = 0.856^{+0.06}_{-0.08} M_\odot$ .

A tight Gaussian prior of  $\pi = 310.94 \pm 0.16$  mas is also imposed on stellar parallax based on the *Hipparcos* parallax measurement for this star (van Leeuwen 2007). We place wide Gaussian priors on the jitter terms, with  $\sigma_j = 10.0 \pm 10.0$  m s<sup>-1</sup>. Large values for jitter are also disfavored by the second term of the likelihood function.

With these priors and this likelihood function, we solve for the full orbital parameters and uncertainties using the Python package *emcee* (Foreman-Mackey et al. 2013). For comparison with the *RadVel* results, we perform our analysis both with and without the direct imaging likelihood. We use planet models of ages 800, 400, and 200 Myr in individual analyses, because the system’s age constraints span this range. We use the standard *emcee* Ensemble Sampler; each MCMC run uses 100 walkers and is iterated for more than 500,000 steps per walker. We check that each sampler satisfies a threshold of Gelman–Rubin statistic  $\hat{R} < 1.1$  for all parameters (Gelman & Rubin 1992; Ford 2006), to test for nonconvergence. We note



**Figure 9.** Corner plot showing the posterior distributions and correlation between the companion mass and inclination for models using the RV likelihood only, as well as RV + direct imaging likelihood with planet models of age 800, 400, and 200 Myr (a log-uniform prior).

that average acceptance fractions for our chains are fairly low,  $\approx 5\%$ – $10\%$ .

#### 4.3.3. MCMC Results

The planet parameters derived in this analysis are consistent with those determined by *RadVel*. The posterior distributions for the companion mass and orbital inclination are plotted in Figure 9. The lower limit on planet mass  $M_b \sin i = 0.72 \pm 0.07 M_{\text{Jup}}$  is constrained by the Keplerian velocity semi-amplitude and agrees well with the *RadVel* results. With the RV data alone, the true mass (independent of  $\sin i$ ) has a poorly constrained upper limit, although high-mass, low-inclination orbits are geometrically disfavored. With the addition of the imaging nondetection constraints, the mass upper limit is improved.

Because younger planets are hotter and thus brighter, the direct imaging likelihood disfavors a broader region of parameter space when a younger age is assumed. Thus, the tightest constraints come from the youngest-aged planet models. Table 4 lists the planet parameters resulting from each MCMC run. We report the median and 68% credible intervals for each model.

We also calculate the posterior distribution on the position of the planet at the epoch of the NIRC2 imaging observation from the RV-only likelihood model. We check this posterior to ensure that the imaging observations were optimally timed to detect the planet at maximal separation from the star. The positional posterior distribution is plotted in Figure 11; it demonstrates that, at the epoch of the imaging observations, the separation of the planet from the star was indeed maximized. The planet would have been easily resolvable, regardless of the on-sky orientation (i.e., the longitude of the ascending node).

For these analyses, we draw companion mass uniformly in logarithmic space with bounds at 0.01 and  $100 M_{\text{Jup}}$ . This is comparable to placing a Jeffreys prior—a common choice of

**Table 4**  
MCMC Results

| Parameter                                       | RV Likelihood Only               | 800 Myr                 | 400 Myr                 | 200 Myr                 |
|---|----------------------------------|-------------------------|-------------------------|-------------------------|
|   | Median and 68% Credible Interval |                         |                         |                         |
| $m_b$ ( $M_{\text{Jup}}$ )                      | $0.78^{+0.43}_{-0.12}$           | $0.78^{+0.38}_{-0.12}$  | $0.75^{+0.19}_{-0.10}$  | $0.71^{+0.09}_{-0.07}$  |
| $P$ (yr)  | $7.37^{+0.07}_{-0.07}$           | $7.37^{+0.07}_{-0.07}$  | $7.37^{+0.07}_{-0.07}$  | $7.38^{+0.07}_{-0.07}$  |
| $e$   | $0.07^{+0.06}_{-0.05}$           | $0.07^{+0.06}_{-0.05}$  | $0.07^{+0.06}_{-0.05}$  | $0.06^{+0.06}_{-0.04}$  |
| $\omega$ ( $^\circ$ )                           | $177^{+49}_{-51}$                | $175^{+53}_{-52}$       | $177^{+48}_{-49}$       | $157^{+66}_{-51}$       |
| $\Omega$ ( $^\circ$ )                           | $180^{+122}_{-123}$              | $184^{+126}_{-131}$     | $212^{+108}_{-148}$     | $276^{+47}_{-158}$      |
| $i$ ( $^\circ$ )                                | $90^{+42}_{-43}$                 | $89^{+42}_{-42}$        | $89^{+35}_{-35}$        | $90^{+23}_{-24}$        |
| $t_{\text{peri}}$ (JD)                          | $2447213^{+336}_{-429}$          | $2447198^{+361}_{-426}$ | $2447218^{+332}_{-407}$ | $2447032^{+475}_{-402}$ |
| $\gamma_{\text{Lick1}}$ ( $\text{m s}^{-1}$ )   | $8.4^{+2.4}_{-2.4}$              | $8.5^{+2.4}_{-2.4}$     | $8.4^{+2.4}_{-2.3}$     | $8.4^{+2.4}_{-2.4}$     |
| $\sigma_{\text{Lick1}}$ ( $\text{m s}^{-1}$ )   | $15.1^{+2.0}_{-1.8}$             | $15.1^{+2.0}_{-1.8}$    | $15.1^{+2.1}_{-1.8}$    | $15.1^{+2.1}_{-1.8}$    |
| $\gamma_{\text{CES+LC}}$ ( $\text{m s}^{-1}$ )  | $6.9^{+2.6}_{-2.6}$              | $6.9^{+2.6}_{-2.6}$     | $6.9^{+2.6}_{-2.6}$     | $6.9^{+2.6}_{-2.5}$     |
| $\sigma_{\text{CES+LC}}$ ( $\text{m s}^{-1}$ )  | $10.9^{+2.5}_{-2.1}$             | $10.9^{+2.5}_{-2.1}$    | $10.9^{+2.5}_{-2.2}$    | $10.9^{+2.5}_{-2.2}$    |
| $\gamma_{\text{Lick2}}$ ( $\text{m s}^{-1}$ )   | $8.5^{+1.9}_{-1.9}$              | $8.5^{+1.9}_{-1.9}$     | $8.5^{+1.9}_{-1.9}$     | $8.5^{+2.0}_{-1.9}$     |
| $\sigma_{\text{Lick2}}$ ( $\text{m s}^{-1}$ )   | $4.7^{+2.1}_{-1.3}$              | $4.7^{+2.2}_{-1.4}$     | $4.7^{+2.1}_{-1.4}$     | $4.8^{+2.2}_{-1.4}$     |
| $\gamma_{\text{Lick3}}$ ( $\text{m s}^{-1}$ )   | $10.5^{+1.9}_{-1.9}$             | $10.6^{+1.8}_{-1.9}$    | $10.5^{+1.9}_{-1.9}$    | $10.6^{+1.9}_{-1.8}$    |
| $\sigma_{\text{Lick3}}$ ( $\text{m s}^{-1}$ )   | $9.2^{+1.4}_{-1.2}$              | $9.2^{+1.4}_{-1.1}$     | $9.2^{+1.4}_{-1.1}$     | $9.2^{+1.4}_{-1.1}$     |
| $\gamma_{\text{CES+VLC}}$ ( $\text{m s}^{-1}$ ) | $3.4^{+1.7}_{-1.8}$              | $3.4^{+1.8}_{-1.9}$     | $3.4^{+1.8}_{-1.8}$     | $3.4^{+1.8}_{-1.8}$     |
| $\sigma_{\text{CES+VLC}}$ ( $\text{m s}^{-1}$ ) | $6.8^{+1.8}_{-1.5}$              | $6.8^{+1.8}_{-1.5}$     | $6.9^{+1.7}_{-1.5}$     | $6.8^{+1.8}_{-1.5}$     |
| $\gamma_{\text{Lick4}}$ ( $\text{m s}^{-1}$ )   | $-2.4^{+1.0}_{-1.0}$             | $-2.4^{+1.0}_{-1.0}$    | $-2.4^{+1.0}_{-1.0}$    | $-2.4^{+1.0}_{-1.0}$    |
| $\sigma_{\text{Lick4}}$ ( $\text{m s}^{-1}$ )   | $8.7^{+0.8}_{-0.7}$              | $8.7^{+0.7}_{-0.7}$     | $8.7^{+0.7}_{-0.7}$     | $8.7^{+0.7}_{-0.7}$     |
| $\gamma_{\text{HARPS}}$ ( $\text{m s}^{-1}$ )   | $-4.5^{+1.6}_{-1.6}$             | $-4.5^{+1.5}_{-1.5}$    | $-4.5^{+1.5}_{-1.5}$    | $-4.4^{+1.6}_{-1.6}$    |
| $\sigma_{\text{HARPS}}$ ( $\text{m s}^{-1}$ )   | $7.4^{+1.3}_{-1.0}$              | $7.4^{+1.3}_{-1.0}$     | $7.4^{+1.3}_{-1.0}$     | $7.4^{+1.3}_{-1.0}$     |
| $\gamma_{\text{HIRES}}$ ( $\text{m s}^{-1}$ )   | $2.0^{+0.9}_{-0.9}$              | $2.0^{+0.9}_{-0.8}$     | $2.0^{+0.9}_{-0.9}$     | $1.9^{+0.9}_{-0.9}$     |
| $\sigma_{\text{HIRES}}$ ( $\text{m s}^{-1}$ )   | $7.9^{+0.7}_{-0.6}$              | $7.8^{+0.7}_{-0.6}$     | $7.9^{+0.7}_{-0.6}$     | $7.8^{+0.6}_{-0.6}$     |
| $\gamma_{\text{APF}}$ ( $\text{m s}^{-1}$ )     | $-2.7^{+1.0}_{-1.0}$             | $-2.7^{+1.0}_{-1.0}$    | $-2.7^{+1.0}_{-1.0}$    | $-2.7^{+1.0}_{-1.0}$    |
| $\sigma_{\text{APF}}$ ( $\text{m s}^{-1}$ )     | $7.3^{+0.5}_{-0.5}$              | $7.3^{+0.5}_{-0.5}$     | $7.3^{+0.5}_{-0.5}$     | $7.3^{+0.5}_{-0.5}$     |

prior for scale parameters such as mass and period (Ford 2006). This prior is also not significantly dissimilar to the mass distribution of Doppler-detected Jovian planets from Cumming et al. (2008), who found that  $\frac{dN}{d \log m} \propto M^{-0.31}$ , a roughly flat distribution in  $\log m$ .

To assess the impact of this choice, we repeat our analysis with a uniform prior on the mass, again from 0.01 to 100  $M_{\text{Jup}}$ . This alternative increases the significance of the tail of the  $m_b$  posterior distribution toward higher masses. Because mass and inclination are highly correlated, this effect also serves to flatten out the inclination posterior, adding more significance to lower-inclination orbits. Figure 10 shows the posteriors and correlation between the mass and inclination of the planet under the modified mass prior. The correlation plot is identical to that shown in Figure 9, and the mass posterior is not qualitatively changed. The median/68% confidence interval planet mass from the 800 Myr model is  $m_b = 0.83^{+0.47}_{-0.15} M_{\text{Jup}}$ , consistent within uncertainties with the mass constraint from the log-mass case at the same age. The inclination posterior has a wider uncertainty in the linear mass case ( $i = 90^\circ \pm 48^\circ$ ) as compared to the log mass case ( $i = 89^\circ \pm 41^\circ$ ). All other orbital and instrumental parameters have equivalent constraints in both cases. We conclude that the prior on mass does not significantly affect the results of the analysis.

## 5. Discussion

In this section, we discuss the impact of our joint RV-direct imaging analysis on the probable age of the system and the possible planet–disk interactions. We also discuss the prospect

of detecting additional planets with future facilities such as the *James Webb Space Telescope*.

### 5.1. Choice of Evolutionary Models

The direct imaging upper limits are model-dependent. We chose to use the COND model mostly for practical reasons. This choice was also motivated by the fact that, at the system’s age and probable planet mass, evolutionary models have mostly forgotten initial conditions such that hot and cold start models have converged (Marley et al. 2007). However, COND is arguably one of the oldest evolutionary models available. The treatment of opacities, chemistry, etc., are all somewhat outdated. For our 800 Myr case, the most probable age for the system, we also generated completeness maps using the evolutionary model presented in Spiegel & Burrows (2012), referred to as SB12 hereafter (Figure 12). Because the publicly available SB12 grid does not fully cover our age and mass range, some minor extrapolations were necessary. The result of this comparison shows some noticeable discrepancies across the range probed by our data (see Figure 12). However, both models seem to agree to within error bars at the location of the planet around 3.48 au, so the impact of the choice of evolutionary model on our joint statistical analysis is only marginal.

### 5.2. Constraints on the System’s Age and Inclination

The planet is not detected in our deep imaging data to the 5 $\sigma$  threshold. According to our upper limits and RV results, the imaging nondetection indicates that the true age of  $\epsilon$  Eridani is

**Table 5**  
Keck Radial Velocity Measurements

| JD            | RV (m s <sup>-1</sup> ) <sup>a</sup> | $\sigma_{RV}$ (m s <sup>-1</sup> ) <sup>b</sup> | $S_{HK}$ |
|---------------|--------------------------------------|---|----------|
| 2455110.97985 | -6.54                                | 1.30  | 0.467    |
| 2455171.90825 | -3.33                                | 1.09  | 0.486    |
| 2455188.78841 | 7.90                                 | 1.11  | 0.481    |
| 2455231.7593  | -8.39                                | 1.13  | 0.497    |
| 2455255.70841 | 1.66                                 | 0.70  | 0.520    |
| 2455260.71231 | 1.77                                 | 1.01  | 0.523    |
| 2455261.71825 | 0.75                                 | 1.30  | 0.526    |
| 2455413.14376 | -10.67                               | 0.76  | 0.500    |
| 2455414.13849 | -16.73                               | 0.99  | 0.000    |
| 2455415.14082 | -20.89                               | 0.78  | 0.495    |
| 2455426.14477 | -17.57                               | 0.86  | 0.494    |
| 2455427.14813 | -18.05                               | 0.87  | 0.483    |
| 2455428.14758 | -21.46                               | 0.87  | 0.480    |
| 2455429.14896 | -18.67                               | 0.90  | 0.475    |
| 2455434.14805 | 7.21                                 | 0.86  | 0.474    |
| 2455435.14705 | 4.46                                 | 0.89  | 0.481    |
| 2455436.14535 | -2.48                                | 0.83  | 0.485    |
| 2455437.15006 | -5.03                                | 0.94  | 0.480    |
| 2455438.15172 | -14.24                               | 0.90  | 0.484    |
| 2455439.14979 | -13.17                               | 0.51  | 0.474    |
| 2455440.15188 | -22.38                               | 0.88  | 0.471    |
| 2455441.15033 | -19.71                               | 0.99  | 0.469    |
| 2455456.01632 | 4.52                                 | 0.97  | 0.466    |
| 2455465.07401 | -12.99                               | 0.98  | 0.449    |
| 2455469.1284  | 7.81                                 | 1.01  | 0.465    |
| 2455471.97444 | -4.15                                | 1.16  | 0.471    |
| 2455487.00413 | -9.44                                | 0.96  | 0.454    |
| 2455500.98687 | -2.23                                | 1.05  | 0.461    |
| 2455521.89317 | -11.42                               | 1.05  | 0.455    |
| 2455542.95125 | -8.56                                | 1.20  | 0.458    |
| 2455613.70363 | 0.65                                 | 1.01  | 0.466    |
| 2455791.13884 | 1.87                                 | 0.87  | 0.433    |
| 2455792.13464 | -9.19                                | 0.90  | 0.430    |
| 2455793.13858 | -17.85                               | 0.89  | 0.426    |
| 2455795.14053 | -15.43                               | 0.96  | 0.418    |
| 2455797.13828 | -5.67                                | 0.83  | 0.419    |
| 2455798.14195 | -5.00                                | 0.84  | 0.424    |
| 2455807.1116  | -3.91                                | 0.99  | 0.417    |
| 2455809.1367  | -0.90                                | 0.99  | 0.429    |
| 2455870.9902  | 1.81                                 | 1.20  | 0.437    |
| 2455902.82961 | 4.20                                 | 0.74  | 0.429    |
| 2455960.69933 | -8.22                                | 1.21  | 0.460    |
| 2456138.12976 | -2.69                                | 0.86  | 0.464    |
| 2456149.05961 | -2.49                                | 0.53  | 0.470    |
| 2456173.13157 | -1.22                                | 0.96  | 0.459    |
| 2456202.99824 | 19.64                                | 0.71  | 0.507    |
| 2456327.70174 | 20.33                                | 1.05  | 0.535    |
| 2456343.7026  | 16.52                                | 1.05  | 0.505    |
| 2456530.11763 | 6.76                                 | 0.90  | 0.489    |
| 2456532.12218 | 8.06                                 | 0.85  | 0.479    |
| 2456587.96668 | 14.41                                | 1.03  | 0.479    |
| 2456613.91026 | 15.04                                | 1.02  | 0.481    |
| 2456637.81493 | 23.88                                | 1.02  | 0.487    |
| 2456638.79118 | 32.35                                | 1.07  | 0.491    |
| 2456674.80603 | 11.70                                | 1.03  | 0.488    |
| 2456708.78257 | 2.49                                 | 0.99  | 0.482    |
| 2456884.13093 | 12.85                                | 0.95  | 0.446    |
| 2456889.14678 | 18.51                                | 0.82  | 0.466    |
| 2456890.14703 | 13.09                                | 0.86  | 0.461    |
| 2456894.13998 | 8.71                                 | 0.83  | 0.446    |
| 2456896.11131 | 15.09                                | 0.78  | 0.447    |
| 2456910.94964 | 13.84                                | 0.64  | 0.450    |
| 2457234.13834 | 9.97                                 | 0.85  | 0.491    |
| 2457240.99109 | 6.26                                 | 0.52  | 0.468    |
| 2457243.14297 | 3.19                                 | 0.78  | 0.476    |

**Table 5**  
(Continued)

| JD            | RV (m s <sup>-1</sup> ) <sup>a</sup> | $\sigma_{RV}$ (m s <sup>-1</sup> ) <sup>b</sup> | $S_{HK}$ |
|---------------|--------------------------------------|---|----------|
| 2457245.14532 | 5.26                                 | 0.90  | 0.479    |
| 2457246.14242 | -1.45                                | 0.99  | 0.477    |
| 2457247.14678 | -5.60                                | 1.01  | 0.482    |
| 2457254.14889 | 8.50                                 | 0.80  | 0.475    |
| 2457255.15244 | 6.36                                 | 0.91  | 0.466    |
| 2457256.15168 | 5.80                                 | 0.83  | 0.476    |
| 2457265.14924 | 5.74                                 | 0.88  | 0.469    |
| 2457291.04683 | 6.07                                 | 1.05  | 0.491    |
| 2457326.9831  | 6.10                                 | 1.12  | 0.501    |
| 2457353.88153 | -0.55                                | 1.09  | 0.519    |
| 2457378.78993 | 2.19                                 | 1.08  | 0.519    |
| 2457384.78144 | 14.17                                | 1.10  | 0.517    |
| 2457401.75106 | 6.07                                 | 0.99  | 0.517    |
| 2457669.02614 | 1.91                                 | 1.10  | 0.497    |
| 2457672.99494 | -1.33                                | 1.20  | 0.497    |
| 2457678.97973 | -13.88                               | 1.10  | 0.495    |
| 2457704.03411 | -14.12                               | 0.67  | 0.501    |
| 2457712.99284 | -4.84                                | 1.18  | 0.478    |
| 2457789.74988 | -13.12                               | 1.12  | 0.439    |
| 2457790.737   | -8.09                                | 1.01  | 0.440    |
| 2457803.70407 | -4.25                                | 1.09  | 0.460    |
| 2457804.70718 | -6.55                                | 1.09  | 0.471    |
| 2457806.79201 | -11.62                               | 1.13  | 0.464    |
| 2457828.7545  | -12.69                               | 1.12  | 0.455    |
| 2457829.71875 | -19.82                               | 0.98  | 0.466    |
| 2457830.71979 | -12.66                               | 1.10  | 0.465    |

**Notes.**<sup>a</sup> The RV data points listed in these tables are not offset-subtracted.<sup>b</sup> Uncertainties quoted in these tables reflect the internal statistical variance of the spectral chunks used to extract the RV data points (see Section 2.2 for a full description). They do not include jitter.

(This table is available in machine-readable form.)

likely to be closer to 800 Myr. Moreover, spectroscopic indicators of age ( $\log R'_{HK}$  and rotation) point toward this star being at the older end of the age range tested here, nearer to 800 Myr than 200 Myr (Mamajek & Hillenbrand 2008). VLTI observations were used to interferometrically measure the stellar radius and place the star on isochrone tracks. These models also yield an age of 800 Myr or more (Di Folco et al. 2004). Thus, the most likely model included here is the 800 Myr model, which is also a fortiori the least restrictive in placing an upper limit on the planet mass. This model yields a mass estimate of  $M_b = 0.78^{+0.38}_{-0.12} M_{Jup}$  and an orbital plane inclination of  $i = 89^\circ \pm 42^\circ$ .

We note that this inclination is marginally consistent with being co-planar with the outer disk belt, which has a measured inclination of  $i = 34^\circ \pm 2^\circ$  (Booth et al. 2017). Although the direct imaging nondetection naturally favors near edge-on solutions, the full posterior distribution can still be interpreted as consistent with the planet being co-planar with the outer disk. With the joint RV and imaging analysis, we are unable to definitively state whether the planet is or is not co-planar with the outer debris disk. However, we are able to rule out ages at or below 200 Myr if coplanarity is required.

To assess the properties of the planet assuming coplanarity with the disk, we repeat our joint analysis, implementing a new Gaussian prior on the inclination of  $i = 34^\circ \pm 2^\circ$  rather than the uninformative geometric prior used in the previous analysis.

**Table 6**  
APF Radial Velocity Measurements

| JD            | RV (m s <sup>-1</sup> ) <sup>a</sup> | $\sigma_{RV}$ (m s <sup>-1</sup> ) <sup>b</sup> | $S_{HK}$ |
|---------------|--------------------------------------|---|----------|
| 2456582.93034 | 26.64                                | 2.73  | 0.524    |
| 2456597.91368 | 6.40                                 | 2.36  | 0.528    |
| 2456606.68427 | 16.52                                | 0.75  | 0.531    |
| 2456608.10376 | 4.69                                 | 0.78  | 0.530    |
| 2456610.7625  | 16.04                                | 1.18  | 0.512    |
| 2456618.88476 | -2.11                                | 0.78  | 0.530    |
| 2456624.72004 | 4.20                                 | 1.11  | 0.519    |
| 2456626.81421 | 24.46                                | 0.75  | 0.521    |
| 2456628.72976 | 24.14                                | 0.70  | 0.540    |
| 2456631.42746 | -2.26                                | 0.88  | 0.502    |
| 2456632.80921 | 14.46                                | 0.62  | 0.523    |
| 2456644.75696 | 8.20                                 | 2.30  | 0.522    |
| 2456647.81171 | 14.44                                | 0.63  | 0.535    |
| 2456648.59184 | 12.62                                | 1.10  | 0.538    |
| 2456662.63738 | 9.77                                 | 0.73  | 0.536    |
| 2456663.75415 | 10.43                                | 1.11  | 0.531    |
| 2456667.52792 | 18.00                                | 0.78  | 0.535    |
| 2456671.68695 | 19.96                                | 1.05  | 0.604    |
| 2456675.75647 | 7.84                                 | 1.12  | 0.519    |
| 2456679.83732 | 17.70                                | 1.05  | 0.529    |
| 2456682.56608 | 17.80                                | 0.82  | 0.550    |
| 2456689.76638 | 26.34                                | 0.75  | 0.500    |
| 2456875.02028 | 7.12                                 | 2.18  | 0.501    |
| 2456894.88054 | 8.28                                 | 1.30  | 0.470    |
| 2456901.06193 | 9.95                                 | 1.54  | 0.479    |
| 2456909.10279 | -4.71                                | 1.21  | 0.476    |
| 2456922.07953 | 12.25                                | 2.13  | 0.461    |
| 2456935.94021 | -2.43                                | 1.27  | 0.479    |
| 2456937.92403 | -0.55                                | 1.35  | 0.468    |
| 2456950.03798 | 3.82                                 | 1.44  | 0.472    |
| 2456985.64755 | -1.80                                | 2.28  | 0.441    |
| 2456988.63095 | 5.93                                 | 1.29  | 0.478    |
| 2456999.76434 | 8.84                                 | 1.37  | 0.459    |
| 2457015.72916 | -2.17                                | 1.10  | 0.465    |
| 2457026.78021 | -1.44                                | 1.34  | 0.464    |
| 2457058.45996 | -3.69                                | 1.89  | 0.435    |
| 2457234.08236 | 7.73                                 | 1.39  | 0.525    |
| 2457245.86234 | -4.19                                | 1.41  | 0.519    |
| 2457249.93007 | -3.94                                | 1.31  | 0.500    |
| 2457253.11257 | 5.63                                 | 1.33  | 0.511    |
| 2457257.15719 | -1.02                                | 1.15  | 0.506    |
| 2457258.94437 | -12.69                               | 1.23  | 0.517    |
| 2457261.02221 | -2.76                                | 1.32  | 0.501    |
| 2457262.94505 | -7.81                                | 1.36  | 0.496    |
| 2457265.95783 | 9.67                                 | 1.24  | 0.516    |
| 2457275.01304 | -1.91                                | 1.23  | 0.515    |
| 2457283.96368 | 1.88                                 | 1.29  | 0.507    |
| 2457287.02735 | -1.11                                | 1.35  | 0.524    |
| 2457290.95635 | 3.19                                 | 1.42  | 0.534    |
| 2457305.83659 | -5.63                                | 1.23  | 0.515    |
| 2457308.90844 | 13.30                                | 1.26  | 0.534    |
| 2457318.83435 | 8.72                                 | 1.26  | 0.557    |
| 2457321.79157 | 6.64                                 | 1.36  | 0.540    |
| 2457325.84352 | 2.87                                 | 1.41  | 0.543    |
| 2457331.10764 | 9.90                                 | 1.36  | 0.552    |
| 2457332.78237 | 9.64                                 | 1.25  | 0.558    |
| 2457334.82998 | 5.22                                 | 1.30  | 0.548    |
| 2457337.7891  | 5.41                                 | 1.59  | 0.545    |
| 2457340.95644 | -1.99                                | 1.27  | 0.553    |
| 2457347.86896 | 4.10                                 | 1.29  | 0.556    |
| 2457348.77993 | 4.65                                 | 1.27  | 0.556    |
| 2457350.72611 | 5.83                                 | 1.20  | 0.558    |
| 2457354.70613 | -0.88                                | 1.65  | 0.548    |
| 2457361.64656 | 17.26                                | 1.43  | 0.549    |

**Table 6**  
(Continued)

| JD            | RV (m s <sup>-1</sup> ) <sup>a</sup> | $\sigma_{RV}$ (m s <sup>-1</sup> ) <sup>b</sup> | $S_{HK}$ |
|---------------|--------------------------------------|---|----------|
| 2457364.77113 | -7.80                                | 1.30  | 0.531    |
| 2457365.70544 | 0.72                                 | 1.26  | 0.550    |
| 2457424.71436 | -1.68                                | 1.37  | 0.555    |
| 2457426.63205 | 3.62                                 | 1.42  | 0.559    |
| 2457427.38923 | 3.97                                 | 1.17  | 0.577    |
| 2457429.72793 | 2.42                                 | 0.90  | 0.560    |
| 2457432.60322 | 6.20                                 | 1.25  | 0.569    |
| 2457435.69406 | -18.61                               | 18.79   | 0.304    |
| 2457443.66061 | 2.25                                 | 1.24  | 0.559    |
| 2457446.70278 | 3.96                                 | 1.37  | 0.566    |
| 2457471.55712 | 5.85                                 | 1.63  | 0.535    |
| 2457599.93545 | -5.69                                | 0.85  | 0.505    |
| 2457605.99828 | -5.33                                | 1.27  | 0.559    |
| 2457607.92844 | -24.97                               | 1.39  | 0.540    |
| 2457611.16197 | -16.02                               | 1.26  | 0.510    |
| 2457613.86777 | 2.47                                 | 1.54  | 0.560    |
| 2457615.04307 | 3.50                                 | 1.48  | 0.538    |
| 2457617.08138 | 0.91                                 | 1.29  | 0.555    |
| 2457619.05397 | -12.30                               | 1.46  | 0.529    |
| 2457621.79772 | -13.43                               | 1.57  | 0.508    |
| 2457626.10874 | 0.39                                 | 1.33  | 0.534    |
| 2457627.95628 | -4.92                                | 1.37  | 0.551    |
| 2457633.96762 | -8.24                                | 1.70  | 0.512    |
| 2457636.08672 | -1.33                                | 1.18  | 0.539    |
| 2457637.95848 | -7.66                                | 1.37  | 0.538    |
| 2457643.92459 | -14.39                               | 1.33  | 0.512    |
| 2457668.93315 | -0.83                                | 1.34  | 0.527    |
| 2457669.90475 | 2.76                                 | 1.43  | 0.533    |
| 2457670.88203 | -8.82                                | 1.42  | 0.543    |
| 2457674.61398 | -5.61                                | 1.42  | 0.534    |
| 2457679.98028 | -12.42                               | 1.78  | 0.515    |
| 2457687.77138 | 1.17                                 | 1.37  | 0.524    |
| 2457694.76122 | -3.81                                | 1.33  | 0.504    |
| 2457696.82099 | -5.60                                | 1.32  | 0.522    |
| 2457700.96748 | -10.84                               | 1.41  | 0.534    |
| 2457701.84849 | -11.69                               | 1.38  | 0.517    |
| 2457702.89789 | -14.82                               | 1.22  | 0.524    |
| 2457703.82658 | -19.89                               | 1.25  | 0.523    |
| 2457705.73282 | -9.58                                | 1.32  | 0.513    |
| 2457707.78376 | -9.03                                | 1.24  | 0.511    |
| 2457717.79818 | -15.06                               | 1.22  | 0.505    |
| 2457722.75749 | -12.43                               | 2.05  | 0.427    |
| 2457728.81592 | -7.64                                | 1.67  | 0.514    |
| 2457741.79955 | -14.52                               | 1.16  | 0.513    |
| 2457743.5028  | -17.28                               | 1.32  | 0.489    |
| 2457745.93451 | -17.74                               | 1.31  | 0.487    |
| 2457749.71344 | -5.63                                | 1.30  | 0.503    |
| 2457751.64976 | -16.16                               | 1.32  | 0.501    |
| 2457753.47716 | -12.45                               | 1.30  | 0.509    |
| 2457798.55461 | -18.91                               | 2.25  | 0.465    |
| 2457821.65582 | -5.60                                | 1.63  | 0.490    |

**Notes.**<sup>a</sup> The RV data points listed in these tables are not offset-subtracted.<sup>b</sup> Uncertainties quoted in these tables reflect the internal statistical variance of the spectral chunks used to extract the RV data points (see Section 2.2 for a full description). They do not include jitter.

(This table is available in machine-readable form.)

We ran this analysis for all of the age models. Each of the models satisfied the convergence criterion for all parameters except for longitude of the ascending node ( $\Omega$ ), which is poorly constrained by our data in all cases. However, the 200 Myr

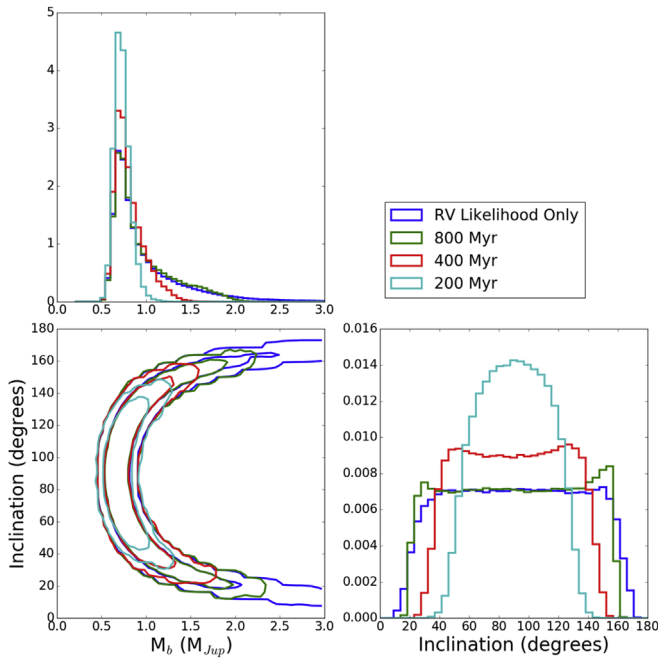


Figure 10. Same as Figure 9, but with uniform prior on companion mass.

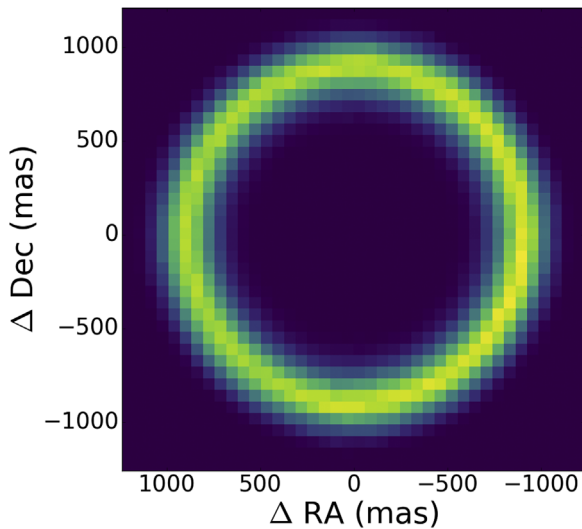


Figure 11. Two-dimensional posterior distribution of the position of the planet during the epoch of the imaging observations. This posterior was produced using the RV likelihood only, and demonstrates that the planet was optimally separated from its host star at the imaging epoch. The values of the pixels in the maximum-likelihood annulus contribute most significantly to the direct imaging likelihood.

model failed to converge in many other parameters, most likely due to the conflict between the youngest models and the coplanarity condition. We therefore report only the 400 Myr and older model results here.

The majority of the fit parameters have posterior distributions consistent with the previous analyses. Because inclination does not correlate strongly with any parameters except companion mass, we do not expect this new prior to affect the posterior probability distributions for any of the other model parameters.

For all age models, the companion mass constraint changes significantly compared to the edge-on orbits preferred by the uninformative prior. The new constraints are all similar to one

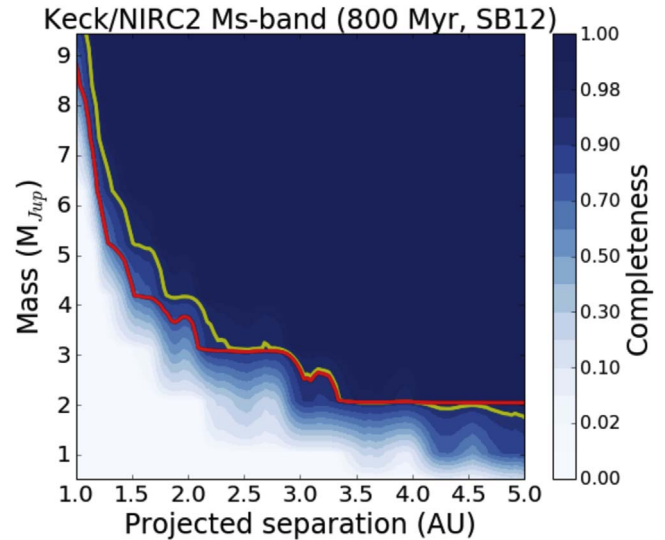


Figure 12. Keck/NIRC2 *Ms*-band vortex performance/completeness map for a  $\tau = 5\sigma$  detection threshold comparing using the SB12 evolutionary model (Spiegel & Burrows 2012). The yellow curve highlights the 95% completeness contour. The red curve highlights the 95% completeness contour for the COND model as in Figure 4.

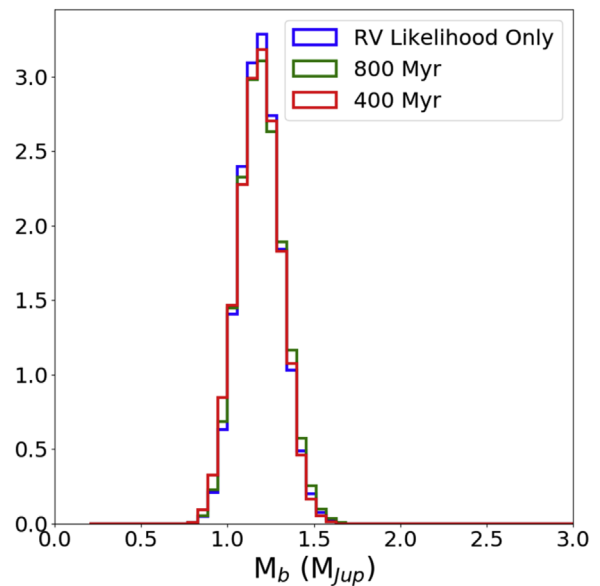


Figure 13. Posterior probability distributions for the mass of  $\epsilon$  Eridani b, when a Gaussian prior preferring orbits coplanar with the measured inclination of the disk ( $i = 34^\circ \pm 2^\circ$ ) is applied instead of the uninformative geometric prior typically used. The resultant distributions are normalized in the plot. The posterior probability distributions are mutually consistent with one another because  $M_b \sin i$  is well-constrained by the RV data. If coplanarity is assumed, the mass of the planet is  $1.19 \pm 0.12 M_J$ .

another, with the exception of the 200 Myr model, which did not achieve convergence. The new median and 68% credible intervals on the planet mass for each model are  $m_b = 1.19 \pm 0.12 M_J$  (RV only),  $1.18^{+0.12}_{-0.11} M_J$  (800 Myr), and  $1.19^{+0.11}_{-0.12} M_J$  (400 Myr). The posterior distributions are plotted in Figure 13.

### 5.3. Planet–disk Interactions

In this section, we investigate the possible connection between  $\epsilon$  Eridani b and the system’s debris belts. Debris disks



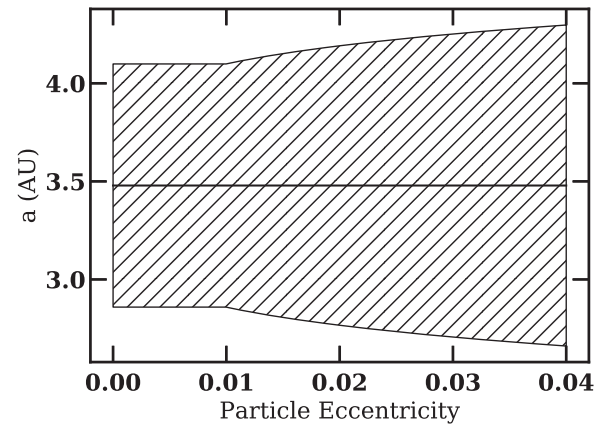
are the leftovers of planet formation and primarily made out of small bodies (asteroids, comets, dust) that are the remnants of planetesimals, the building blocks of planet cores. Debris disks can be traced by the intrinsic thermal emission of micron-sized particles generated in collisional cascades between the small bodies. For some favorable geometries, scattering of the small particles can also be detected at optical wavelengths. The dust is constantly replenished by the collisions between leftover planetesimals that are gravitationally stirred by themselves or by neighboring planets. Non-axisymmetric features and separated rings revealed in scattered light images and/or thermal emissions of micron-sized to millimeter-sized dust particles are considered signposts of existing planets. The connection between debris disks and planets has been seen in several of the currently known, directly imaged planetary systems, such as HR 8799,  $\beta$  Pictoris, HD 95086, HD 106906, Fomalhaut, and 51 Eridani (see, e.g., Bowler (2016) for a recent review). Using the largest sample of debris disks systems directly surveyed for long-period giant planets to date, Meshkat et al. (2017) recently found that the occurrence rate of long-period giant planets in dusty systems is about ten times higher than in dust-free systems (88% confidence level), providing the first tentative empirical evidence for a planet–disk connection.

### 5.3.1. Constraining the Inner Belt(s)

Armed with refined orbital parameters of  $\epsilon$  Eridani b, we place constraints on the inner belt(s) identified by Su et al. (2017). Close to the planet, inside a chaotic zone, an overlap of mean motion resonances destabilizes the orbits of particles on short timescales, effectively clearing them out (e.g., Wisdom 1980; Quillen & Faber 2006; Morrison & Malhotra 2015). Wisdom (1980) showed that the width of the chaotic zone scales with  $\mu^{2/7}$ , where  $\mu$  is the mass ratio between the planet and the star. Quillen & Faber (2006) find that the width of the chaotic zone is independent of planet eccentricity  $e_{\text{pl}}$ , as long as  $e_{\text{pl}} \lesssim 0.3$ . We have shown that  $\epsilon$  Eridani b has an eccentricity consistent with zero and definitively smaller than 0.3. Using the numerically calibrated expressions for the chaotic zone’s inner edge  $(1 - 1.17 \mu^{0.28})a_{\text{pl}}$  and the outer edge  $(1 + 1.76 \mu^{0.31})a_{\text{pl}}$  where  $a_{\text{pl}}$  is the semimajor axis of the planet (see Morrison & Malhotra 2015, their Table 1), we find that  $\epsilon$  Eridani b would clear out 2.90–4.19 au if the planet was located at 3.48 au (equivalent to a  $0.78 M_{\text{Jup}}$  planet orbiting a star of  $0.78 M_{\odot}$  at orbital periods of 7.37 yr; see the “800 Myr” column of Table 4).

If the particles within the planetesimal belts have sufficiently large free eccentricities (i.e., initial eccentricities set by self-stirring and collision; see, e.g., Pan & Schlichting (2012)), the chaotic zone can widen, commensurate with the particle eccentricities (Mustill & Wyatt 2012). For  $\epsilon$  Eridani b, the critical particle eccentricity is only  $\sim 0.21 \mu^{3/7} \sim 0.01$ . In Figure 14, we show that, for particles more eccentric than  $\sim 0.01$ , the chaotic zone around  $\epsilon$  Eridani b can widen by a few tens of percent.

Overall, we expect there to be no particles between  $\sim 2.7$  and  $\sim 4.3$  au. If the excess IR emission interior to 25 au is from one broad disk, its inner edge must be beyond  $\sim 4.3$  au. If instead the excess emission is from two narrow belts, the innermost belt must be inside  $\sim 2.7$  au while the outermost belt must be outside  $\sim 4.3$  au. Both scenarios are roughly consistent with the analysis of Su et al. (2017) and the most recent LBTI results (Ertel et al. 2018).



**Figure 14.** The chaotic zone around  $\epsilon$  Eridani b as a function of particle free eccentricity. The hatched zone corresponds to the chaotic zone around the most likely location of the planet ( $a = 3.48$  au; horizontal solid line). The planet mass is fixed to  $0.78 M_{\text{Jup}}$ . We expect the region between  $\sim 2.7$  and  $\sim 4.3$  au to be cleared out by  $\epsilon$  Eridani b.

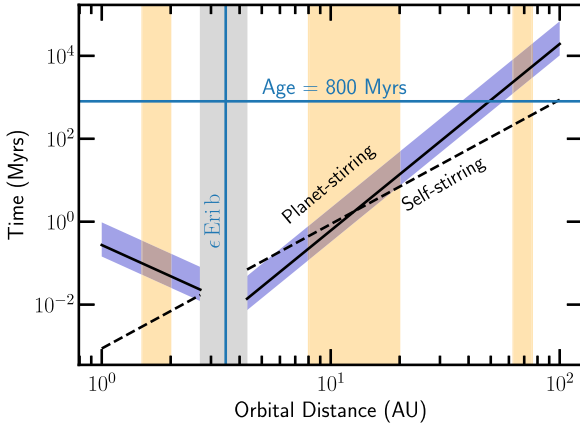
### 5.3.2. Dust Production in Planetesimal Belts: Planet-stirred or Self-stirred?

Dust grains that are millimeter-sized and smaller that dominate the radio and scattered light images are the products of collisions among larger planetesimals. Particles can collide with each other as they gravitationally stir each other or they may be secularly perturbed by a planet. Is  $\epsilon$  Eridani b responsible for triggering collisional cascades in the warm and cold belts detected in the system, or are the planetesimals more likely to be self-stirred?

The characteristic timescale for planetesimals to stir each other is set by their rate of collision (see, e.g., Section 4.1.4 of Goldreich et al. (2004)). Numerical (e.g., Kenyon & Bromley 2008) and analytic (e.g., Pan & Schlichting 2012) calculations suggest bodies as large as  $\sim 1000$  km are at the top of the collisional cascade: they can stir up smaller bodies to disruption at a rate faster than their growth via accretion. It is the formation timescale of these Pluto-sized bodies that limits the overall self-stirring timescale:

$$t_{\text{ss}} \sim 173 \text{ Myr} \left( \frac{\Sigma_{\text{MMSN}}}{\Sigma} \right)^{1.15} \left( \frac{a_{\text{disk}}}{60 \text{ au}} \right)^3 \left( \frac{M_{\odot}}{M_{\star}} \right)^{3/2}, \quad (10)$$

where  $a_{\text{disk}}$  is the semimajor axis of the planetesimals,  $M_{\star}$  is the mass of the host star,  $\Sigma_{\text{MMSN}} \equiv 0.18 \text{ g cm}^{-2} (M_{\star}/M_{\odot}) (a/30 \text{ au})^{-3/2}$  is the Minimum Mass Solar Nebula (MMSN), and we take the coefficient derived by numerical simulations of Kenyon & Bromley (2008). The calculation above assumes large bodies build up mostly after the dispersal of the gas disk, because gas dynamical friction tends to damp away the eccentricities of solids. It may be that planetesimals are built rapidly even in the early stages of gas disk evolution—by streaming instability (e.g., Youdin & Goodman 2005; Johansen et al. 2007), resonant drag instability (Squire & Hopkins 2018), and/or pebble accretion (e.g., Ormel & Klahr 2010; Ormel 2017)—such that Pluto-sized bodies are already available by the time the disk gas dissipates. Without the need to wait for the build-up of large bodies after the gas dispersal,  $t_{\text{ss}}$  can be shortened by an order of magnitude (Krivov & Booth 2018).



**Figure 15.** The timescale for  $\epsilon$  Eridani b to stir particles at different distances (Equations (11) and (12)) compared against the self-stirring timescale (Equation (10)). The blue bar reflects the range of eccentricities of  $\epsilon$  Eridani b from our MCMC analysis, with the lower and upper limit corresponding to  $e_{\text{pl}} = 0.13$  and  $e_{\text{pl}} = 0.02$ , respectively; the solid line represents the median  $e_{\text{pl}} = 0.07$ . We fix  $M_{\text{pl}} = 0.78 M_{\text{Jup}}$ ,  $a_{\text{pl}} = 3.48$  au, and  $M_{\star} = 0.78 M_{\odot}$ . We have assumed MMSN surface density to calculate the self-stirring timescale. The expected chaotic zone of  $\epsilon$  Eridani b is depicted with a gray zone. Three orange bars illustrate the warm and cold belts reported by Su et al. (2017) and Booth et al. (2017), respectively. Unless  $\epsilon$  Eridani’s disk is significantly less massive than MMSN—by more than an order of magnitude—it is likely that the collisions within the innermost warm belt and the outermost cold belt are driven by self-stirring rather than the secular perturbation by  $\epsilon$  Eridani b. Collisions in the secondary warm belt that span 8–20 au are consistent with both self-stirring and planet-stirring.

The orbit crossing timescale for two nearby planetesimals as they are secularly perturbed by a planet is  $t_{\text{cross}} \sim 1/Ae_p$  where  $A$  is the precession frequency and  $e_p$  is the eccentricity of the perturbed particle (Mustill & Wyatt 2009). For particles on initially circular orbits,  $e_p$  is set by the forced eccentricity such that the orbit-crossing timescale becomes

$$t_{\text{cross}} \approx 500 \text{ Gyr} \frac{(1 - e_{\text{pl}}^2)^{3/2}}{e_{\text{pl}}} \left( \frac{a_{\text{disk}}}{60 \text{ au}} \right)^{9/2} \times \left( \frac{M_{\star}}{M_{\odot}} \right)^{1/2} \left( \frac{M_{\text{Jup}}}{M_{\text{pl}}} \right) \left( \frac{3.5 \text{ au}}{a_{\text{pl}}} \right)^3 \quad (11)$$

for internal perturbers, and

$$t_{\text{cross}} \approx 17.4 \text{ kyr} \frac{(1 - e_{\text{pl}}^2)^{3/2}}{e_{\text{pl}}} \left( \frac{a_{\text{pl}}}{3.5 \text{ au}} \right)^4 \times \left( \frac{M_{\star}}{M_{\odot}} \right)^{1/2} \left( \frac{M_{\text{Jup}}}{M_{\text{pl}}} \right) \left( \frac{1 \text{ au}}{a_{\text{disk}}} \right)^{5/2} \quad (12)$$

for external perturbers, where  $e_{\text{pl}}$  is the planet eccentricity,  $M_{\text{pl}}$  is the planet mass, and  $a_{\text{pl}}$  is the semimajor axis of the perturbing planet (see Mustill & Wyatt (2009), their Equations (15) and 16). For  $\epsilon$  Eridani b to be responsible for the dust production in planetesimal belts,  $t_{\text{cross}}$  must be shorter than the age of the system and  $t_{\text{cross}} < t_{\text{ss}}$ . For our refined parameters for  $\epsilon$  Eridani b, we find that, out of the three belts that are imaged or inferred to exist, the innermost and the outermost belts are more likely self-stirred, while the intermediate warm belt can be either self-stirred or planet-stirred (see Figure 15).

Even the self-stirring timescale for the outer belt is uncomfortably close to the system’s estimated age. It may be that the largest bodies that trigger a collisional cascade emerge

rapidly, such that our  $t_{\text{ss}}$  is overestimated. It may also be that an extra planet beyond the orbit of  $\epsilon$  Eridani b is responsible for stirring the outermost belt and for carving out the region between the inner warm belts and the outer cold belt. Our solution with uninformative inclination priors to the orbit of  $\epsilon$  Eridani b favors an orbital inclination ( $89^{\circ} \pm 42^{\circ}$ ) that is larger than the inclination of the outermost belt ( $34^{\circ} \pm 2^{\circ}$ ). Such a large misalignment suggests that  $\epsilon$  Eridani may have interacted with a fly-by in the past and/or there exists another planet that is inclined to the orbit of  $\epsilon$  Eridani b.

Should this extra planet be responsible for tilting the outer belt from the orbital plane of  $\epsilon$  Eridani b, we expect its orbit to be misaligned with respect to  $\epsilon$  Eridani b by at least  $10^{\circ}$ , assuming the mass of the extra planet is  $\sim 1$  Jupiter mass with an orbital distance of 48 au.

In Meshkat et al. (2017), we found that the occurrence rate of long-period planets in debris disks is about 10 times higher than in dust-free systems. The  $\epsilon$  Eridani system is rich in dust contained in multiple belts reminiscent of the HR 8799 system (Su et al. 2009), so it may very well harbor more than one planet, as suggested by previous studies (Mizuki et al. 2016; Booth et al. 2017). Unfortunately, the field of view of our high-contrast Keck/NIRC2 data set is too small to probe a large separation in the vicinity of the outer disk.

### 5.3.3. Imaging the Elusive $\epsilon$ Eridani Planet(s) with JWST

The Keck/NIRC2  $M_s$ -band vortex coronagraph high-contrast images presented here showcase an exquisite inner working angle ( $0''.2$ ) and sensitivity up to  $5''$ . Ground-based adaptive optics and small-angle coronagraphy in the mid-infrared (from 3 to  $5 \mu\text{m}$ ) on 10 m class telescopes will only be challenged by the advent of Giant Segmented Mirror Telescopes (GSMTs). However, NIRC2 and MIRI, the infrared cameras of the upcoming *James Webb Space Telescope*, will have unmatched sensitivity beyond  $1''$  from the star. Thus, *JWST*’s NIRC2 and MIRI are ideal instruments to explore the inner cavity of  $\epsilon$  Eridani from 3 to  $30 \mu\text{m}$ , and reveal additional elusive planets. The outer ring being at  $20''$  from the host star, the diffraction and scattering from the star will be less of a concern, allowing us to probe the cavity for the putative planet shepherding the outer ring. Invoking dynamical arguments similar to those used in the previous sections and upper limits from *Spitzer* images (Janson et al. 2015), Booth et al. (2017) predict that the putative exoplanet responsible for shaping the outer belt is at a semimajor axis of 48 au, with a mass between 0.4 and  $1.2 M_J$ .

*JWST*’s NIRC2 instrument team is planning coronagraphic observations at  $4.4 \mu\text{m}$  (F444W) to search both the interior ( $\pm 10''$ ) and exterior regions ( $2''.2$ ) around  $\epsilon$  Eridani for planets. The interior region will be observed twice to reject background objects on the basis of source motion, while the entire field will be observed at  $3 \mu\text{m}$  to reject background stars and galaxies on the basis of color. The expected contrast ratio after roll and reference star subtraction is expected to be  $\sim 10^{-6}$  at  $1''$  and  $\sim 10^{-7}$  at  $2''$ , depending on the in-orbit stability of *JWST* (Krist et al. 2007; Beichman et al. 2010).

As noted above, translating between instrumental detection limits and planet mass is challenging due to the uncertainties in stellar age and exoplanet models at low masses. For a nominal age of 800 Myr, the SB12 and COND models yield F444W brightness estimates ranging from 16 to 18 mag for a  $0.78 M_{\text{Jup}}$  planet (effective temperature of  $\simeq 150$  K). In the most favorable

case (SB12), NIRCcam could detect  $\epsilon$  Eridani b at  $1''$  (close to the nominal 7.37 yr, 3.48 au orbit) with S/N  $\sim 5$  and beyond  $2''$  with S/N  $> 25$ . Within  $1''$ , the Keck observations reported here are comparable to or more sensitive than planned *JWST* observations due to Keck's larger aperture and the improved performance of the vortex coronagraph. At larger separations, however, the low thermal background in space gives *JWST* a significant advantage to look for  $< 0.5 M_{\text{Jup}}$  planets (depending on model assumptions) that might be responsible for the disk structures seen in the far-infrared and by ALMA. Because the field of view of both NIRCcam and MIRI is  $20'' \times 20''$ , at least two pointings will be necessary to map out the inner cavity at the vicinity of the outer ring.

## 6. Conclusion

In this paper, we have presented the most sensitive and comprehensive observational evidence for the existence of  $\epsilon$  Eridani b. Combining exquisite RV and direct imaging data provides unprecedented constraints on the mass and orbital parameters of the planet.  $\epsilon$  Eridani b has a mass of  $0.78^{+0.38}_{-0.12} M_{\text{Jup}}$  and is orbiting  $\epsilon$  Eridani at about  $3.48 \pm 0.02$  au in  $7.37 \pm 0.07$  yr. Assuming coplanarity with the outer belt resolved by ALMA (inclination of  $34^\circ \pm 2^\circ$ ), the mass of the planet is approximately  $1.19 M_{\text{Jup}}$ . Our data and analysis also present compelling lines of evidence that the system's age is closer to 800 Myr or more. Indeed, the direct imaging data should have shown the planet if the system's age was 200 Myr. Notably, we also find that the eccentricity of  $\epsilon$  Eridani b is a very low,  $0.07^{+0.06}_{-0.05}$ , an order of magnitude smaller than early estimates and consistent with a circular orbit. For that reason and using simple dynamical arguments, we postulate that  $\epsilon$  Eridani b is unlikely to be responsible for stirring the outer debris belt at 70 au, and that one or more additional planets must be shepherding it. However,  $\epsilon$  Eridani b could be responsible for shaping the putative warm belt(s) within 25 au, although self-stirring is another likely dust production mechanism. If any additional planets exist, they will be easily detected with *JWST*'s NIRCcam and MIRI from 4 to 25  $\mu\text{m}$ , enabling unique spectroscopic and dynamical characterization opportunities.

This paper also demonstrates the unique power of the combination of RV and direct imaging observations to detect and constrain the masses of giant planets within 10 au. The long history of RV observations limited the spatial domain in which  $\epsilon$  Eridani b could reside, allowing optimized detectability with the imaging observations.

We would be remiss if we did not mention as a caveat that the direct imaging nondetection of the planet leaves open the possibility, however small, that the planet does not actually exist. Although there is no obvious commensurability between the long-term magnetic activity diagnostic ( $S_{\text{HK}}$ ) and the RV data, as demonstrated in Section 4.2, it remains possible that the magnetic field affects the RVs in a way we do not understand.

$\epsilon$  Eridani remains a fascinating testbed for studying planetary formation in great detail. We conclude this paper by emphasizing the perfect complementarity between long-term RV monitoring, mid-infrared small-angle high-contrast ground-based capabilities, and the sensitive space-based parameter space to be opened by *JWST*.

The authors would like to acknowledge the contributions and useful comments from Prof. Debra Fischer and Prof. James Graham. The data presented herein were obtained at the W.M. Keck Observatory, which is operated as a scientific partnership among the California Institute of Technology, the University of California, and the National Aeronautics and Space Administration (NASA). The Observatory was made possible by the generous financial support of the W.M. Keck Foundation. The authors wish to recognize and acknowledge the very significant cultural role and reverence that the summit of Maunakea has always had within the indigenous Hawaiian community. We are most fortunate to have the opportunity to conduct observations from this mountain. This work was partially performed at the Jet Propulsion Laboratory, California Institute of Technology, under contract with NASA. (C) 2017. All rights reserved. E.C. acknowledges support from NASA through Hubble Fellowship grant HF2-51355 awarded by STScI, which is operated by AURA, Inc. for NASA under contract NAS5-26555. We also acknowledge support from NASA/NExSS through grant no. NNX15AD95G.

*Software:* RadVel (Fulton et al. 2018), emcee (Foreman-Mackey et al. 2013), VIP (Gomez Gonzalez et al. 2017), PyKLIP (Wang et al. 2015).

## ORCID iDs

Dimitri Mawet  <https://orcid.org/0000-0002-8895-4735>  
 Lea Hirsch  <https://orcid.org/0000-0001-8058-7443>  
 Eve J. Lee  <https://orcid.org/0000-0002-1228-9820>  
 Jean-Baptiste Ruffio  <https://orcid.org/0000-0003-2233-4821>  
 Michael Bottom  <https://orcid.org/0000-0003-1341-5531>  
 Benjamin J. Fulton  <https://orcid.org/0000-0003-3504-5316>  
 Olivier Absil  <https://orcid.org/0000-0002-4006-6237>  
 Brendan Bowler  <https://orcid.org/0000-0003-2649-2288>  
 Marta Bryan  <https://orcid.org/0000-0002-6076-5967>  
 Elodie Choquet  <https://orcid.org/0000-0002-9173-0740>  
 Denis Defrère  <https://orcid.org/0000-0003-3499-2506>  
 Carlos Alberto Gomez Gonzalez  <https://orcid.org/0000-0003-2050-1710>  
 Andrew W. Howard  <https://orcid.org/0000-0001-8638-0320>  
 Howard Isaacson  <https://orcid.org/0000-0002-0531-1073>  
 Rebecca Jensen-Clem  <https://orcid.org/0000-0003-0054-2953>  
 Molly Kosiarek  <https://orcid.org/0000-0002-6115-4359>  
 Geoff Marcy  <https://orcid.org/0000-0002-2909-0113>  
 Tiffany Meshkat  <https://orcid.org/0000-0001-6126-2467>  
 Erik Petigura  <https://orcid.org/0000-0003-0967-2893>  
 Maddalena Reggiani  <https://orcid.org/0000-0003-2911-0898>  
 Garreth Ruane  <https://orcid.org/0000-0003-4769-1665>  
 Evan Sinukoff  <https://orcid.org/0000-0002-5658-0601>  
 Ji Wang  <https://orcid.org/0000-0002-4361-8885>  
 Lauren Weiss  <https://orcid.org/0000-0002-3725-3058>

## References

- Anglada-Escudé, G., & Butler, R. P. 2012, *ApJS*, 200, 15  
 Aumann, H. H. 1985, *PASP*, 97, 885  
 Backman, D., Marengo, M., Stapelfeldt, K., et al. 2009, *ApJ*, 690, 1522  
 Baraffe, I., Chabrier, G., Barman, T. S., Allard, F., & Hauschildt, P. H. 2003, *A&A*, 402, 701  
 Beichman, C. A., Krist, J., Trauger, J. T., et al. 2010, *PASP*, 122, 162

- Beuzit, J.-L., Feldt, M., Dohlen, K., et al. 2008, *Proc. SPIE*, 7014, 701418
- Booth, M., Dent, W. R. F., Jordán, A., et al. 2017, *MNRAS*, 469, 3200
- Bowler, B. P. 2016, *PASP*, 128, 102001
- Boyajian, T. S., von Braun, K., van Belle, G., et al. 2012, *ApJ*, 757, 112
- Butler, R. P., Marcy, G. W., Williams, E., et al. 1996, *PASP*, 108, 500
- Chavez-Dagostino, M., Bertone, E., Cruz-Saenz de Miera, F., et al. 2016, *MNRAS*, 462, 2285
- Cox, A. N. 2000, *Allen's astrophysical quantities* (4th; Melville, NY: AIP)
- Cumming, A., Butler, R. P., Marcy, G. W., et al. 2008, *PASP*, 120, 531
- Di Folco, E., Thévenin, F., Kervella, P., et al. 2004, *A&A*, 426, 601
- Ducati, J. R. 2002, *yCat*, 2237, 0
- Ertel, S., Defrère, D., Hinz, P., et al. 2018, *AJ*, 155, 194
- Fischer, D. A., Marcy, G. W., & Spronck, J. F. P. 2014, *ApJS*, 210, 5
- Ford, E. B. 2006, *ApJ*, 642, 505
- Foreman-Mackey, D., Hogg, D. W., Lang, D., & Goodman, J. 2013, *PASP*, 125, 306
- Fortney, J. J., Marley, M. S., Saumon, D., & Lodders, K. 2008, *ApJ*, 683, 1104
- Fuhrmann, K. 2004, *AN*, 325, 3
- Fulton, B. J., Petigura, E. A., Blunt, S., & Sinukoff, E. 2018, *PASP*, 130, 044504
- Gelman, A., & Rubin, D. B. 1992, *StaSc*, 7, 457
- Goldreich, P., Lithwick, Y., & Sari, R. 2004, *ARA&A*, 42, 549
- Gomez Gonzalez, C. A., Wertz, O., Absil, O., et al. 2017, *AJ*, 154, 7
- Greaves, J. S., Holland, W. S., Moriarty-Schieven, G., et al. 1998, *ApJL*, 506, L133
- Greaves, J. S., Holland, W. S., Wyatt, M. C., et al. 2005, *ApJL*, 619, L187
- Greaves, J. S., Sibthorpe, B., Acke, B., et al. 2014, *ApJL*, 791, L11
- Grunblatt, S. K., Howard, A. W., & Haywood, R. D. 2015, *ApJ*, 808, 127
- Hatzes, A. P., Cochran, W. D., McArthur, B., et al. 2000, *ApJL*, 544, L145
- Howard, A. W., & Fulton, B. J. 2016, *PASP*, 128, 114401
- Howard, A. W., Johnson, J. A., Marcy, G. W., et al. 2010, *ApJ*, 721, 1467
- Howard, A. W., Marcy, G. W., Fischer, D. A., et al. 2014, *ApJ*, 794, 51
- Huby, E., Baudoz, P., Mawet, D., & Absil, O. 2015, *A&A*, 584, A74
- Huby, E., Bottom, M., Femenia, B., et al. 2017, *A&A*, 600, A46
- Isaacson, H., & Fischer, D. 2010, *ApJ*, 725, 875
- Janson, M., Quanz, S. P., Carson, J. C., et al. 2015, *A&A*, 574, A120
- Jensen-Clem, R., Mawet, D., Gomez Gonzalez, C. A., et al. 2018, *AJ*, 155, 19
- Johansen, A., Oishi, J. S., Mac Low, M.-M., et al. 2007, *Natur*, 448, 1022
- Jovanovic, N., Martinache, F., Guyon, O., et al. 2015, *PASP*, 127, 890
- Keenan, P. C., & McNeil, R. C. 1989, *ApJS*, 71, 245
- Kenyon, S. J., & Bromley, B. C. 2008, *ApJS*, 179, 451
- Krist, J. E., Beichman, C. A., Trauger, J. T., et al. 2007, *Proc. SPIE*, 6693, 66930H
- Krivov, A. V., & Booth, M. 2018, *MNRAS*, 479, 3300
- López-Morales, M., Haywood, R. D., Coughlin, J. L., et al. 2016, *AJ*, 152, 204
- MacGregor, M. A., Wilner, D. J., Andrews, S. M., Lestrade, J.-F., & Maddison, S. 2015, *ApJ*, 809, 47
- Macintosh, B., Graham, J. R., Ingraham, P., et al. 2014, *PNAS*, 111, 12661
- Mamajek, E. E., & Hillenbrand, L. A. 2008, *ApJ*, 687, 1264
- Marley, M. S., Fortney, J. J., Hubickyj, O., Bodenheimer, P., & Lissauer, J. J. 2007, *ApJ*, 655, 541
- Marois, C., Lafrenière, D., Doyon, R., Macintosh, B., & Nadeau, D. 2006, *ApJ*, 641, 556
- Marois, C., Lafrenière, D., Macintosh, B., & Doyon, R. 2008, *ApJ*, 673, 647
- Mawet, D., Choquet, É., Absil, O., et al. 2017, *AJ*, 153, 44
- Mawet, D., Milli, J., Wahhaj, Z., et al. 2014, *ApJ*, 792, 97
- Mawet, D., Riaud, P., Absil, O., & Surdej, J. 2005, *ApJ*, 633, 1191
- Meshkat, T., Mawet, D., Bryan, M., et al. 2017, *AJ*, 154, 245
- Mizuki, T., Yamada, T., Carson, J. C., et al. 2016, *A&A*, 595, A79
- Morrison, S., & Malhotra, R. 2015, *ApJ*, 799, 41
- Mustill, A. J., & Wyatt, M. C. 2009, *MNRAS*, 399, 1403
- Mustill, A. J., & Wyatt, M. C. 2012, *MNRAS*, 419, 3074
- Ormel, C. W. 2017, in *Formation, Evolution, and Dynamics of Young Solar Systems*, Astrophysics and Space Science Library, Vol. 445, ed. M. Pessah & O. Gressel (Switzerland: Springer International), 197
- Ormel, C. W., & Klahr, H. H. 2010, *A&A*, 520, A43
- O'Toole, S. J., Tinney, C. G., Jones, H. R. A., et al. 2009, *MNRAS*, 392, 641
- Pan, M., & Schlichting, H. E. 2012, *ApJ*, 747, 113
- Pueyo, L. 2016, *ApJ*, 824, 117
- Quillen, A. C., & Faber, P. 2006, *MNRAS*, 373, 1245
- Radovan, M. V., Lanclus, K., Holden, B. P., et al. 2014, *Proc. SPIE*, 9145, 91452B
- Ruffio, J.-B., Macintosh, B., Wang, J. J., et al. 2017, *ApJ*, 842, 14
- Ruffio, J.-B., Mawet, D., Czekala, I., et al. 2018, *AJ*, 156, 196
- Serabyn, E., Huby, E., Matthews, K., et al. 2017, *AJ*, 153, 43
- Soummer, R., Pueyo, L., & Larkin, J. 2012, *ApJL*, 755, L28
- Spiegel, D. S., & Burrows, A. 2012, *ApJ*, 745, 174
- Squire, J., & Hopkins, P. F. 2018, *MNRAS*, 477, 5011
- Stevenson, D. J. 1991, *ARA&A*, 29, 163
- Su, K. Y. L., De Buizer, J. M., Rieke, G. H., et al. 2017, *AJ*, 153, 226
- Su, K. Y. L., Rieke, G. H., Stapelfeldt, K. R., et al. 2009, *ApJ*, 705, 314
- Takeda, G., Ford, E. B., Sills, A., et al. 2007, *ApJS*, 168, 297
- Valenti, J. A., & Fischer, D. A. 2005, *ApJS*, 159, 141
- van Leeuwen, F. 2007, *A&A*, 474, 653
- Vargas Catalán, E., Huby, E., Forsberg, P., et al. 2016, *A&A*, 595, A127
- Vogt, S. S., Allen, S. L., Bigelow, B. C., et al. 1994, *Proc. SPIE*, 2198, 362
- Vogt, S. S., Radovan, M., Kibrick, R., et al. 2014, *PASP*, 126, 359
- Walker, H. J., & Heinrichsen, I. 2000, *Icar*, 143, 147
- Wang, J. J., Ruffio, J.-B., De Rosa, R. J., et al. 2015, pyKLIP: PSF Subtraction for Exoplanets and Disks, Astrophysics Source Code Library, ascl:1506.001
- Wisdom, J. 1980, *AJ*, 85, 1122
- Youdin, A. N., & Goodman, J. 2005, *ApJ*, 620, 459
- Zechmeister, M., Kürster, M., & Endl, M. 2009, *A&A*, 505, 859
- Zechmeister, M., Kürster, M., Endl, M., et al. 2013, *A&A*, 552, A78